

Solid-Phase Epitaxy

Brett C. Johnson¹, Jeffrey C. McCallum¹, Michael J. Aziz²

¹SCHOOL OF PHYSICS, UNIVERSITY OF MELBOURNE, VICTORIA, AUSTRALIA; ²HARVARD
SCHOOL OF ENGINEERING AND APPLIED SCIENCES, CAMBRIDGE, MA, USA

CHAPTER OUTLINE

7.1 Introduction and Background.....	318
7.2 Experimental Methods.....	319
7.2.1 Sample Preparation.....	319
7.2.1.1 Heating.....	321
7.2.2 Characterization Methods.....	321
7.2.2.1 Time-Resolved Reflectivity.....	321
7.2.2.2 Other Techniques.....	323
7.3 Solid-Phase Epitaxy in Si and Ge.....	323
7.3.1 Structure of Materials.....	323
7.3.1.1 Relaxed Amorphous Si and Ge.....	326
7.3.1.2 Deposited Amorphous Si and Ge.....	326
7.3.1.3 Crystal-Amorphous Interface.....	326
7.3.2 Intrinsic SPE.....	327
7.3.3 Orientation Dependence.....	329
7.3.4 Pressure Dependence.....	331
7.3.4.1 Hydrostatic Pressure.....	331
7.3.4.2 Nonhydrostatic Stress.....	332
7.3.4.3 Interface Roughening.....	334
7.3.5 Ion Beam-Induced Epitaxial Crystallization.....	335
7.3.6 Dopant Dependence.....	336
7.3.6.1 Dopant-Induced Strain.....	339
7.3.7 Dopant Activation.....	341
7.4 Atomistic Models.....	342
7.4.1 Construction of Materials.....	343
7.4.2 Monte Carlo Simulations of Solid-Phase Epitaxy.....	343
7.4.3 Molecular Dynamics Simulations of Solid-Phase Epitaxy.....	345
7.5 Defects Formed during Solid-Phase Epitaxy.....	348

7.6 Diffusion and Segregation of Impurities during Solid-Phase Epitaxy	351
7.6.1 Dopants	351
7.6.2 Nondoping Impurities.....	352
7.6.3 Metals.....	353
7.7 SPE in Other Semiconductors	354
7.8 Summary	355
Acknowledgments	356
References	356

7.1 Introduction and Background

Solid-phase epitaxy, or SPE, takes place when a metastable amorphous material is in intimate contact with a crystalline substrate. When heated, atoms in the amorphous phase reorder by local bond rearrangements at the crystalline–amorphous (*c–a*) interface. This process takes place entirely in the solid state, and the resultant structure mimics the underlying crystalline substrate, which acts as a template. Other than thermal heating, the process can also be induced by laser, electron, or ion irradiation [1]. Figure 7.1 shows the growth of crystal germanium (Ge) after various partial thermal anneals.

A SPE rate can be associated with the propagation of the *c–a* interface through the amorphous layer and is often described by an Arrhenius-type equation of the form [3]

$$v = v_o \exp(-E_a/kT) \quad (7.1)$$

where E_a is the activation energy and v_o the velocity prefactor. The SPE interface can reach rates of more than 100 $\mu\text{m/s}$. Attempts have been made to link the activation energy to some feature of the *c–a* interface or defect that assists in the bond rearrangement process that accompanies SPE.

Such models address SPE on a number of different fronts. One approach has been to consider the atomistic nature of the SPE process (i.e., how the atoms on the *a*-Si side of the interface are rearranged onto the crystal template). The other is based on kinematic

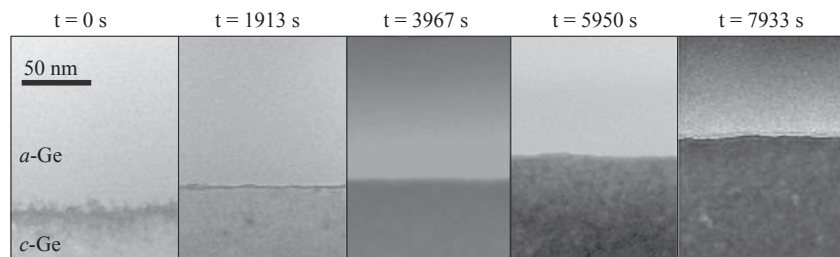


FIGURE 7.1 Cross-section transmission electron microscopic images of germanium (Ge) showing the movement of the crystalline (*c*)–amorphous (*a*) interface toward the surface after anneals at 310 °C for the durations indicated [2]. *t* = time. Reprinted from Ref. [2] with permission from Elsevier.

considerations. These models attempt to identify the rate-limiting step of the SPE process and derive an expression that can predict the SPE rate as a function of various experimental conditions.

A number of excellent review articles exist that describe the early development of the field since the first reports in 1968 by Mayer et al. [4] onward [5,6]. These reviews include an outline of many of the parameters that affect SPE growth kinetics, such as temperature, pressure, crystal orientation, and impurity concentration. More recently, new theoretical and experimental techniques have been developed that have greatly enhanced our understanding of SPE and the experimental parameters that affect it. SPE has long been an important processing step in device fabrication, and it continues to be so [7]. It aids in the electrical activation of dopant atoms and the removal of damage. Active dopant concentrations in excess of the solid solubility limit can be achieved. It is also a relatively low-temperature process and is therefore compatible with a broad range of other device fabrication processes and materials, such as high-K dielectrics and metal gates. With the continual downscaling of semiconductor devices and the search for new materials with unique and useful functionalities, there is a drive to understand and refine further our knowledge of SPE kinetics.

In this chapter, recent progress in SPE studies is reviewed. The main material systems considered are silicon (Si) and Ge, given their technological importance. Although Si still dominates the semiconductor industry, Ge has increased in technological importance, especially with the advent high-K dielectrics and incorporation of heterostructures and strain engineering for both optical and electrical applications. Ge is also compatible with Si complementary metal oxide semiconductor (CMOS) processing and is an interesting system to compare with Si. There is also now sufficient new information regarding Ge SPE to warrant its detailed review alongside Si. Such a comparison also has the potential to provide important insight into the atomic rearrangement processes responsible for SPE.

7.2 Experimental Methods

7.2.1 Sample Preparation

High-fluence ion implantation and film deposition are the most common methods used to form an amorphous layer in contact with a crystalline template for subsequent SPE growth. Ion implantation is an indispensable tool for the fabrication of semiconductor devices and is used routinely to modify the surface properties of materials [8,9]. Atomic displacements via primary and secondary knock-ons are caused by nuclear stopping processes in a crystal, resulting in the formation of damage cascades.

With continual bombardment, cascades and their eventual overlap can result in the formation of continuous amorphous layers. The kinetics of this process are sensitive to the accumulation of damage, the implanted ion energy, fluence, current, and sample temperature. After a certain threshold ion fluence is exceeded, the crystal becomes amorphous, with no long-range atomic order. The thickness of the amorphous layer

depends primarily on the initial energy of the implanted ions. The exact depth range of the ions is well modeled by Monte Carlo (MC) codes like Stopping and Range of Ions in Matter (SRIM) [10] and crystal-TRansport of Ions in Matter (c-TRIM) [11].

Dynamic processes taking place during implantation such as defect formation and diffusion remains an active area of investigation. One such phenomenon of note is the formation of porous layers in implanted Ge [12–14]. This occurs via the generation and clustering of vacancies in the amorphous *a*-Ge phase. This process may result in deleterious device behavior arising from an increase in surface roughness, swelling of the implanted region, absorption of contaminants resulting from the increased surface area, and changes in conductivity [15,16]. The formation of the porous layer can usually be avoided if the sample is held at a low temperature (typically 80 K) during implantation. This ensures the damage is frozen and the clustering of vacancies is suppressed. However, if heavy ions such as Antimony (Sb) are implanted, the porous layer still forms even at low temperatures [17,18]. SPE kinetics in the amorphous layer beyond the depth of the porous layer are not affected significantly.

A broad range of deposition techniques are also available to form amorphous layers on a crystalline seed template. They include Plasma Enhanced Chemical Vapour Deposition [19], evaporation [20], sputtering chemical vapor deposition, physical vapor deposition, Metal-Organic Chemical Vapour Deposition, and Molecular Beam Epitaxy. The advantage of depositing on an amorphous layer is that the substrate need not have the same elemental composition. Provided that the lattices are well matched, a single crystal layer can be grown. These methods result in amorphous materials that may contain high concentrations of impurities or voids that may retard SPE growth.

The geometry of the amorphous layer comes in a wide variety of forms depending on the preparation methods, and can have a large impact on SPE kinetics and the resulting crystal layer quality. Figure 7.2(a) shows the planar configuration often used for SPE experiments. The *c*-*a* interface is planar, so that the velocity can be measured easily.

Commercial devices are now on the nanometer scale, and processing steps may involve the amorphization of spatially confined regions usually defined by a surface mask (Figure 7.2(B)) followed by SPE anneals [21–23]. It can be seen that, in this case, the *c*-*a* interface is no longer planar, and this has a significant impact on the resulting crystal, with SPE proceeding in more than one direction. Freestanding or amorphous layers encapsulated in another material such as a dielectric are also possible

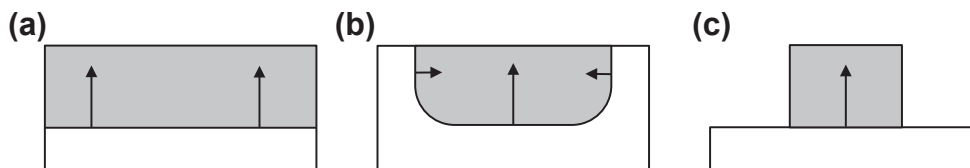


FIGURE 7.2 (a–c) Sample configurations for standard solid-phase epitaxy studies (a), shallow junction formation (b) and seeded growth (c).

(Figure 7.2(c)). Lateral SPE—where growth of a thin amorphous layer on a silicon dioxide (SiO_2) surface proceeds laterally and is seeded by an opening in the SiO_2 so that contact is made with the underlying substrate—is another possible geometry [24]. This method has been used to prepare Si on insulator structures.

7.2.1.1 Heating

After an amorphous layer has been formed, SPE may be induced by a variety of heating methods, including furnace, rapid thermal, flash lamp, and laser annealing. The method used depends on the available thermal budget and impurity considerations. Being a thermally activated process, reasonable time frames to observe SPE anneals take place at temperatures as low as 500 °C for Si and 350 °C for Ge. For temperatures greater than 700 °C, measurements of the SPE rate require laser heating, so the target temperature is reached before a complete transformation takes place. Rapid thermal annealing is also often used to reduce diffusion and out-diffusion of implanted dopants while also achieving a high dopant activation.

7.2.2 Characterization Methods

7.2.2.1 Time-Resolved Reflectivity

Time-resolved reflectivity (TRR) is an extremely reliable and accurate method of measuring the SPE rate in amorphous layers with relatively large lateral dimensions. TRR makes use of the difference in refractive index between the amorphous and crystalline phases. Interference between reflections from the sample surface and the buried c - a interface can be monitored during interface motion. It is possible to detect as little as 1–2 nm of interface motion through the change of the net reflectivity with time [5].

To calculate the interface velocity from a raw reflectivity measurement, the theoretical reflectivity trace must first be calculated as a function of a -Si layer thickness. This is achieved by evaluating the theoretical expression for the reflectivity from a thin film on an infinitely thick underlying substrate, [5]

$$R = \left| \frac{r_{01} + r_{12}e^{-\alpha\Delta x}e^{-i2k\Delta x}}{1 + r_{01}r_{12}e^{-\alpha\Delta x}e^{-i2k\Delta x}} \right|^2, \quad (7.2)$$

where Δx is the amorphous layer thickness, α is the absorption coefficient, and k is the wave number coefficient. These are expressed as

$$\alpha = \frac{4\pi}{\lambda} \text{Im}(N) \quad (7.3a)$$

$$k = \frac{2\pi}{\lambda} \text{Re}(N) \quad (7.3b)$$

where $\text{Im}(N)$ and $\text{Re}(N)$ are the real and imaginary parts of the refractive index. The terms, r_{ij} , in Eqn (7.2) are the Fresnel reflection coefficients and can be written as

$$r_{ij} = \frac{N_j - N_i}{N_j + N_i} \quad (7.4)$$

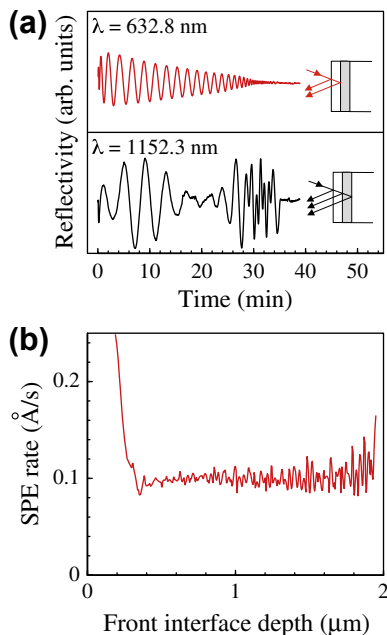


FIGURE 7.3 (a, b) Time-resolved reflectivity trace of a silicon sample containing a buried amorphous layer annealed at 500 °C collected with both 632.8-nm (a) and 1152.3-nm (b) lasers. The infrared laser signal is a convolution of reflections off the surface and the front and back crystalline–amorphous interfaces. Sample geometries are shown in the inset. The velocity (b) of the front interface as it moves deeper into the sample extracted from the visible trace in (a). SPE, solid-phase epitaxy. arb., arbitrary.

The real and imaginary parts of the refractive index are known to vary with temperature and can be calculated using the empirical relations of Jellison and Modine [25] for *c*-Si and Olson and Roth [5] for *a*-Si. Jellison and Modine’s formulae were obtained from fits to data over the 35–490 °C temperature range, and they are still valid for the 460–660 °C temperature range of standard SPE experiments [26].

The use of TRR for measurements of SPE rates of surface *a*-Si layers are well described in [6]. For more complex layer structures, such as buried *a*-Si layers, collection of the reflectivity traces at two well-chosen wavelengths can provide valuable information [27]. For example, Figure 7.3 shows typical TRR traces for a buried *a*-Si sample annealed at 500 °C. The visible laser has a short penetration depth into *a*-Si, so only information about the receding *c*–*a* interface is obtained. To obtain the SPE velocity-versus-depth profile in Figure 7.3(b), Eqn (7.2) is used to obtain a reflectivity-versus-depth curve. This is compared with the TRR trace, and a depth-versus-time profile is obtained. Through differentiation and a conversion of the *x*-axis, the required profile is obtained. The initial velocity is fast as a result of the sharpening of the interface, but drops quickly to a constant value. At greater depths, as the TRR oscillation contrast decreases, the noise becomes greater. This contrast can also be modified by changes in the *c*–*a* interface roughness, the nucleation and growth of polycrystalline material, or the growth of

extended defects at the interface [28,29]. The TRR trace obtained with the near infrared laser is complicated because the reflectivity trace results from interference between reflections from three interfaces: the surface and the moving front and back interfaces of the *a*-Si layer.

7.2.2.2 Other Techniques

Several other characterization techniques are important for gaining insight into SPE and related processes. In particular, before the advent of TRR, Rutherford backscattering spectroscopy and ion channeling (RBS-C) was often used to determine the interface velocity by measuring amorphous layer thicknesses after anneals of various durations. Although this technique is not generally an in situ technique and does not have a comparable depth resolution, the depth distribution and concentration of impurity atoms and their lattice location can be determined [30–32].

Both TRR and RBS-C have limitations on the minimum amorphous layer thickness from which accurate data can be obtained. A full TRR oscillation corresponds to a depth of $\lambda/2n$, so at least half of this thickness is required to extract SPE rates comfortably. Of course the wavelength can be decreased for greater depth resolution, but the absorption depth of the laser also decreases. When using a 633-nm laser with surface *a*-Si layers, this amounts to $\lambda/4n \approx 40$ nm. If the exact thickness is already known, a fraction of this depth (~ 10 nm) can be studied using TRR. Investigations on amorphous layers of these thicknesses and thinner are becoming important, for example, in the fabrication of shallow junctions. Therefore, other characterization methods are becoming important, such as transmission electron microscopy (TEM; an example of which is given in Figure 7.1).

7.3 Solid-Phase Epitaxy in Si and Ge

7.3.1 Structure of Materials

Before considering the SPE process, the crystalline and amorphous structures and the interface between them need to be defined. For crystalline Si and Ge, the four valence electrons bond covalently with four nearest neighbors in a tetrahedral configuration, resulting in a diamond cubic lattice composed of sixfold rings in a “chair” configuration shown in Figure 7.4 [33]. The nearest neighbors are separated by a distance of $a\sqrt{3}/4$, where the characteristic lattice constants are $a_{\text{Si}} = 0.543$ nm and $a_{\text{Ge}} = 0.566$ nm. The angle between any two adjacent tetrahedral bonds is 109.47° .

The structure of the amorphous phase is not as easily defined and, in fact, has long been the subject of considerable debate. Its properties are dependent on the method of fabrication and the thermal history of the sample, and its atomic structure is extremely difficult to determine experimentally. In general, the long-range order that characterizes the crystal lattice is absent, and only short- and medium-range order is retained. With the lack of translational symmetry, the amorphous solid is instead characterized by the

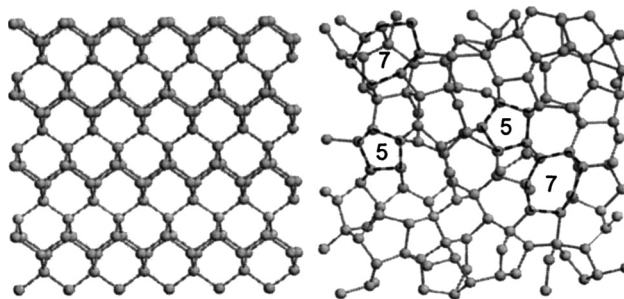


FIGURE 7.4 Model of the crystalline and continuous random network structure. Reprinted with permission from Ref. [33]. Copyright (2004), AIP Publishing LLC.

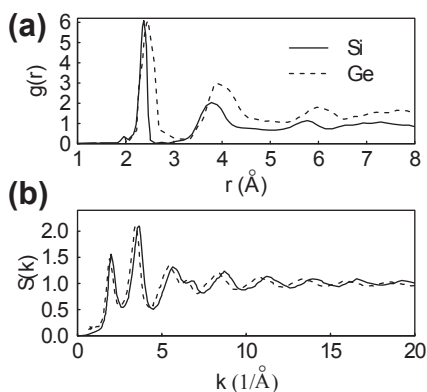


FIGURE 7.5 (a, b) Experimental pair correlation function (a) and structure factor (b) of amorphous silicon (Si) and germanium (Ge). Data from Refs [34,35].

pair correlation function (PCF) (Figure 7.5(a)), which indicates the probability per unit volume to find an atom between spheres of radius r and $r + dr$ centered on any atom:

$$g(r) = \frac{G(r)}{4\pi r^2 \rho_0} \quad (7.5)$$

where ρ_0 is the average density of atoms and $G(r)$ is the radial distribution function,

$$G(r) = \frac{1}{N} \sum_{ij} \delta(r - |R_i - R_j|) \quad (7.6)$$

where $|R_i - R_j|$ is the distance between atoms i and j , and N is the total number of atoms. The maxima in Figure 7.5(a) correspond to the positions of the nearest neighbors out to about 1 nm. Such curves can be obtained from conventional diffraction experiments. For monoatomic systems like amorphous Si and Ge, they provide information about the short-range order, not medium-range order. The structure factor, $S(k)$, displayed for Si and Ge in Figure 7.5(b) is related to the PCF via a Fourier transform and can, in principle, be obtained from the reduced diffraction data.

The definition of short-range order also includes bond lengths, coordination number, and bond angle ranges. These are all in the first to second coordination sphere and are on the less than 1-nm-length scale. Techniques such as TEM are most sensitive within this range, albeit not without some ambiguity. Because TEM images of samples with a finite thickness are two-dimensional (2D) representations of a three-dimensional structure, atoms lying along the electron beam axis may be far apart but will have an apparent structural correlation [36].

Medium-range order is characterized by higher order correlations such as dihedral angles (four-body correlations) and ring statistics, which are associated with the 1–3-nm-length scale. These structural correlations are expected to be subtle and are not apparent in TEM data. Other techniques such as fluctuation electron microscopy, a hybrid imaging/diffraction technique, have been developed to address this regime [37]. Correlations greater than 3 nm are not known for amorphous semiconductors and are more characteristic of polycrystalline materials.

Given that no single technique is able to provide information on all levels of atomic correlation, modeling and comparative analysis studies have thus been instrumental in developing a detailed understanding of the overall amorphous structure [38–40]. Observables such as the PCF or phonon density of states are common benchmarks against which simulated structures are compared. By far the most common model is the continuous random network (CRN) in which, in addition to the sixfold rings characteristic of *c*-Si, five- and sevenfold rings also exist [41]. A 2D representation of these ring structures is compared with *c*-Si in Figure 7.4. According to the CRN, each atom has four nearest neighbors in an approximate tetrahedral arrangement and is fully coordinated. This arrangement results in short-range order. The lack of long-range order is achieved through small variations in tetrahedral bond angles (109.5° with a root mean square deviation of 10°) and lengths (2.35 \AA) and the relative rotation of adjacent tetrahedra.

Although the CRN model is widely used to understand amorphous semiconductors and is supported by numerous X-ray, electron, and neutron beam diffraction studies, alternative models have been developed to understand the medium-range order, with an early example being the microcrystalline model. Instead of atoms being linked together in a random manner to form networks that do not exhibit long-range periodicity, this model considers amorphous systems to consist of arbitrarily oriented microcrystalline cells separated by disordered layers [42]. Experimental results indicate there are no crystallite sizes with dimensions greater than 15–20 \AA (<400 atoms). This model was developed further into cluster-type models, in which these small crystallites are replaced by clusters [43] or amorphons [44] of hundreds of atoms arranged in a regular noncrystalline configuration. Last, the paracrystalline model has seen some sway in describing fluctuation electron microscopy results [37] [45–47]. However, the difficulty in definitively establishing one model over another means that modeling remains controversial [47,48]. The construction of amorphous models is discussed further in Section 7.4.1.

7.3.1.1 *Relaxed Amorphous Si and Ge*

The structure of *a*-Si and *a*-Ge produced by ion implantation is known to be modified by thermal annealing below the crystallization temperature and produces a more “relaxed” amorphous structure. This modification is accompanied by a reduction in the free energy of the material and has been linked to both short-range ordering and the annihilation of defects in the amorphous structure [49–51]. This implies that the structure of *a*-Si cannot be described fully by the CRN model, because up to one atomic percent of defects (5×10^{20} defects/cm³) exist in the *a*-Si structure.

Structural relaxation is known to lower the diffusion coefficients of various impurities in *a*-Si. However, the impact of relaxation on the SPE kinetics appears to be negligible [52,53]. This suggests that the defects that are annihilated during relaxation are not involved in the rate-limiting step of the SPE process.

7.3.1.2 *Deposited Amorphous Si and Ge*

There are significant differences between amorphous layers produced by ion implantation and deposited films [54]. Amorphous Si produced by ion implantation has a well-defined and reproducible set of characteristics, and is independent of the implantation conditions. It is also 1.8% less dense than *c*-Si [55], and the absence of nanovoids has been demonstrated to a sensitivity of 0.1 vol.% [56]. The formation of *a*-Si by deposition contains a high concentration of hydrogen (H; typically 10–20 at.%). The effect of this is that the dangling bonds present in this *a*-Si:H material are passivated, unpinning the Fermi level and allowing doping for device applications. Because of H, these films also contain low-density inhomogeneities that are thought to be voids or H-rich clusters [57]. The behavior of H thus has a significant impact over the structural and electrical properties of the material, and continues to be an area of active research. H retards SPE regrowth and is considered in detail in Section 7.6.2.

7.3.1.3 *Crystal–Amorphous Interface*

At the interface between the crystalline and amorphous phases, the bonds are thought to be fully coordinated [58]—that is, there are no free bonds, so it is in the lowest energy configuration. This is illustrated by Spaepen’s ball-and-stick model of the {111} interface, even in the presence of <110> ledges [58–60]. There may be a small number of defects at the interface, but most of the excess strain resulting from matching the amorphous and crystalline structures is carried by slightly greater distortions in bond angles and weaker bonds than in the bulk of the amorphous phase itself [60]. The spatial transition zone from the amorphous-to-crystalline phase has been determined theoretically by a number of authors, with results in the range 3–11 Å thick for Si [61–63]. Therefore, the interface is quite sharp where there are a few layers between the two phases having intermediate properties (e.g., coordination, enthalpy). However, the interface can also be characterized by a roughness that may be affected by the orientation of the crystal (e.g., [64]). Spaepen’s ball-and-spring model indicated that major topological rearrangements at the interface, such as bond breaking and reformation, could convert the five-, six-, and

sevenfold rings of the amorphous structure into the sixfold chairs of the crystalline structure [65].

7.3.2 Intrinsic SPE

Crystalline Si has a lower Gibbs free energy per atom (G) than the amorphous semi-conducting phase under all realized experimental conditions. The rate at which the amorphous phase transforms to the crystalline phase is so low at temperatures up to a few 100 °C that a -Si may be used in long-lived practical devices; but, with increasing temperatures greater than approximately $T_{\text{Si}} = 500$ °C or $T_{\text{Ge}} = 350$ °C, crystallization occurs with increasing rapidity. The crystallization kinetics are well described by classic theories of nucleation and growth. In the presence of a preexisting c - a interface, nucleation is unnecessary, in which case the transformation is often entirely determined by the rate of SPE.

The growth rate is well described by modeling it as a simple thermally activated process with an energy barrier, in which an atom, or a collection of atoms, undergoes a transition from the amorphous structure to the crystal structure at the c - a interface [52,65–68]. This is illustrated in Figure 7.6, where ΔG_{ac} is the Gibbs free energy difference per atom between the amorphous and crystalline states and ΔG^* is the free energy barrier to crystallization. Both of these quantities depend on temperature and pressure according to well-known thermodynamic relations. The number of transitions per site per second at which an amorphous-to-crystal transition occurs is given by

$$k^+ = \nu \exp(-\Delta G^*/kT), \quad (7.7)$$

where ν is the attempt frequency [68]. The number of transitions per site per second in the reverse direction, k^- , is given by the same expression, except with a larger barrier height, $\Delta G^* + \Delta G_{ac}$.

The SPE rate v_{ac} is then the product of the areal density of interfacial sites at which a transition may occur, the volume transformed per transition, and the net transition

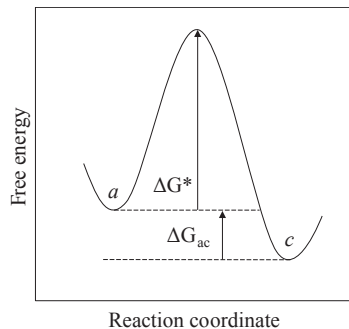


FIGURE 7.6 Schematic of the Gibbs free energy (not to scale) versus reaction coordinate representing the energetics of a transformation between the amorphous and crystalline phases. The activation energy, ΔG^* , is 2.70 eV for silicon and 2.15 eV for germanium.

rate $k^+ - k^-$. The SPE rate, which is the velocity at which the interface moves, is thus given by

$$v = v_\infty \exp(-\Delta H^*/kT)(1 - \exp(-\Delta G_{ac}/kT)), \quad (7.8)$$

where ΔH^* is the activation enthalpy, kT has the usual meaning, and we have collected into v_∞ the preexponential factors, including the exponential of the activation entropy. Because the thermodynamic factor $(1 - \exp(-\Delta G_{ac}/kT))$ hardly varies over experimentally accessible conditions [69], we may also gather it into the preexponential factor, resulting in

$$v = v_o \exp(-\Delta H^*/kT). \quad (7.9)$$

At normal pressures, $\Delta H^* = \Delta E^* + P\Delta V^*$ is indistinguishable from the “activation energy” ΔE^* , which is, in shorthand, called E_a in Eqn (7.1).

For Si(001) the activation energy and preexponential factor are $E_a = 2.7$ eV and $v_o = 4.64 \times 10^6$ m/s, respectively. For Ge(001) they are $E_a = 2.15$ eV and $v_o = 2.6 \times 10^7$ m/s, respectively [70,71]. According to this equation, crystallization occurs at rates from 0.1 to 10,000 Å/s for temperatures in the range 500–800 °C for Si and 315–530 °C for Ge, as shown in Figure 7.7.

The specific atomistic process or processes characterized by these activation energies have never been identified definitively. By assuming that an atom can become part of the crystal when it has at least two nearest neighbors already in crystalline positions, Csepregi et al. [72] argued that growth would occur by the lateral spread of {111} terraces at the c - a interface. This is shown schematically in Figure 7.8. The actual event leading to SPE regrowth has been proposed to occur at kink sites on $\langle 110 \rangle$ ledges on {111} oriented terraces, causing kink migration as indicated by the white arrows in Figure 7.8 [73].

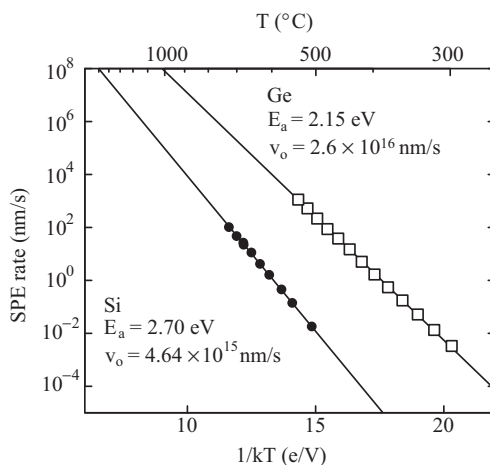


FIGURE 7.7 Solid-phase epitaxy (SPE) rate as a function of $1/kT$ for silicon (Si) [70] and germanium (Ge) [71] as obtained from time-resolved reflectivity measurements.

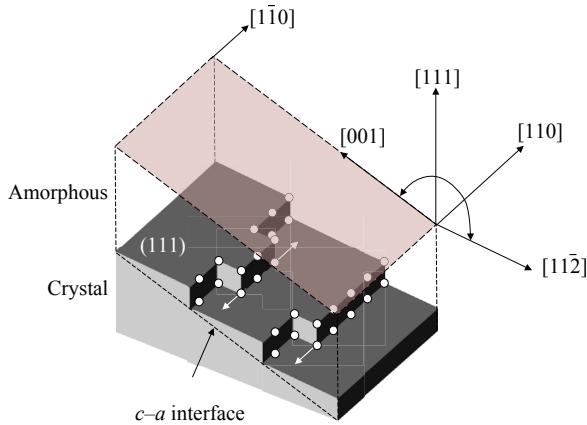


FIGURE 7.8 Schematic of $[1\bar{1}0]$ ledge structure at the crystalline–amorphous (c – a) interface consisting of layered (111) planes for a substrate deviating from [111] in the direction of [110]. Kink migration occurs along the ledges, as indicated by the white arrows. The projected plane shows the orientation of the c – a interface, with major crystallographic directions indicated.

For the CRN to convert to the sixfold chair structure of the crystal, bond breaking and rearrangement must occur. It is possible to make major topological readjustments with the breaking of just one interfacial bond and the propagation of the resulting pair of dangling bonds along the interface [58,59]. Dangling bond breaking and propagation provide the simplest mechanism for kink site motion that is consistent with the atomistic models and the SPE data, including the observation of a single activation energy over ten orders of magnitude of variation in SPE rate. However, molecular dynamics (MD) simulations provide a less clear picture and indicate that a range of cooperative motions of atoms and bonds may also be involved, as discussed in Section 7.4.3.

7.3.3 Orientation Dependence

The SPE rate and the quality of the resulting substrate depend strongly on the interface orientation. Figure 7.9 shows the SPE rate versus the misorientation from (111) for both Si and Ge. The growth rate is 25 times faster when growing on a {001} crystal than on a {111} crystal [72]. Although there are large changes in the SPE rate, the activation energies do not vary with orientation; this suggests that the underlying SPE mechanism does not change (Figure 7.10).

Csepregi et al. [72] noted a $\sin(\theta)$ dependence of the SPE rate on orientation, which has fair agreement with the data in Figure 7.9. As can be seen, for crystal orientations deviating away from [111] toward the [011] direction, the SPE rates are underestimated and require a different scaling factor. As noted by Spaepen and Turnbull [76] this difference can be explained by the different nature of the $[1\bar{1}0]$ ledges involved. For example, for ledges involving deviations from [111] to [110], only one bond is connected to the amorphous phase whereas ledges arising from [111] to [100] deviations have two. Custer [77] developed a different model based on the bond density across the c – a interface (solid line in Figure 7.9) that provides the best fit to the available data.

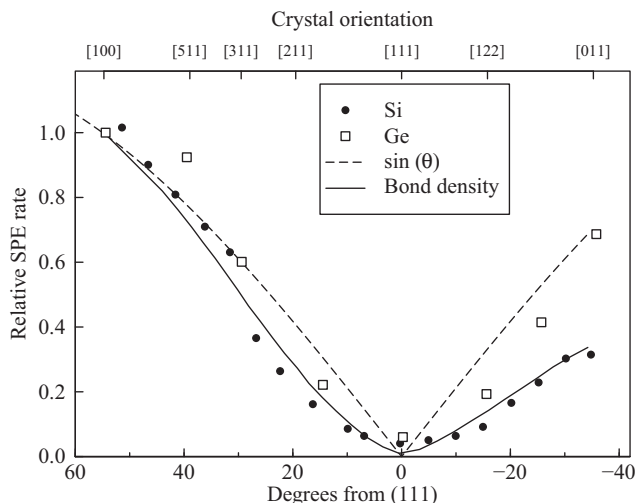


FIGURE 7.9 Normalized solid-phase epitaxy (SPE) rate versus the interface misorientation from (111). (*Silicon (Si) data (550 °C) from Ref. [72] and germanium (Ge) from Ref. [74]. The solid line is the relative dangling bond density between the crystal and amorphous phases [75].*

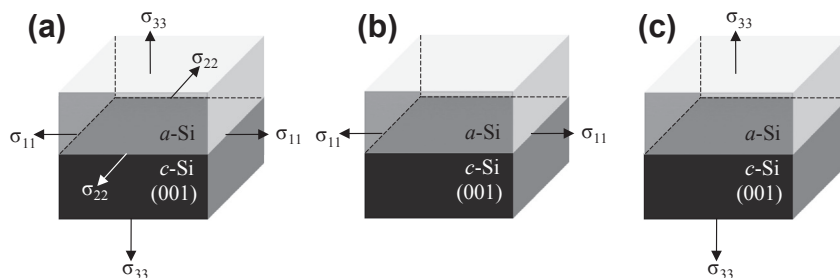


FIGURE 7.10 (a–c) Schematic of (100) silicon (Si) solid-phase epitaxy growth where the crystalline (c)–amorphous (a) interface is moving upward. The application of compression is represented by the arrows for the hydrostatic (a), in-plane uniaxial (b), and normal uniaxial cases (c) [84]. After Ref. [84].

SPE in substrates very near the $\{111\}$ orientation result in an imperfect crystal containing a significant density of defects [78]. The SPE rate on $\{111\}$ crystals is nonlinear with time, exhibiting a slow initial stage of growth followed by a faster stage [79]. The latter stage is dominated by the formation of twin defects inclined to the surface and associated with the $\langle 511 \rangle$ orientation, which is a much faster growth direction than $\{111\}$. This may be the cause of the nonlinear behavior [72,80,81]. Such defects are not as prevalent in Ge, and only a linear growth mode is observed in $\{111\}$ SPE in Ge [74].

The orientation dependence of phosphorus (P)- and boron (B)-enhanced SPE has also been considered by Ho et al. [80]. Crystals grown on a doped (111) substrate were found to have a better crystal quality than undoped samples resulting from the suppression of competing twin formations.

7.3.4 Pressure Dependence

Strains of up to 1 GPa can exist during device fabrication [82]. For example, silicon nitride (SiN) overlayers on Si devices cause stress in the underlying substrate in an inhomogeneous way during fabrication [83]. Therefore, the effect of stress is an important consideration in device fabrication. At the same time, hydrostatic pressure and spatially uniform, nonhydrostatic stress are convenient thermodynamic variables that can be used to test our fundamental understanding of SPE. The derivative of the SPE rate with respect to changes in temperature, pressure, and macroscopically imposed stress states may be interpreted directly in terms of the activation enthalpy, volume, and strain, respectively. These may be interpreted as the changes in the enthalpy, volume, and shape of the system on surmounting the barrier to the transition state [52,67,69].

7.3.4.1 Hydrostatic Pressure

Early reports of stress effects on SPE involved the application of hydrostatic pressure [52,85,86]. Because $\partial G(T,P)/\partial P = V$, Eqn (7.7) leads to

$$v(P) = v(0)\exp(-P\Delta V^*/kT) \quad (7.10)$$

where P is the applied hydrostatic pressure (as depicted in Fig. 7.10) and ΔV^* is the activation volume. Lu et al. [52,85] measured the Si and Ge SPE rate dependence on hydrostatic pressure. Figure 7.11 shows the results for Ge(001) at several annealing temperatures. The exponential enhancement with pressure is consistent with a negative activation volume of $\Delta V^* = -0.46 \Omega_{\text{Ge}}$, where $\Omega_{\text{Ge}} = 13.6 \text{ cm}^3/\text{mole}$ is the atomic volume of Ge. Similarly, the exponential enhancement measured in Si is characterized by $\Delta V^* = -0.28 \pm 0.03 \Omega_{\text{Si}}$, where $\Omega = 12.1 \text{ cm}^3/\text{mol}$. The negative activation volume is consistent with an SPE mechanism involving dangling bond migration, in which the transition state is a dangling bond reaching across a ring to attack a fully coordinated atom, thereby making it an overcoordinated atom. Hydrostatic pressure makes it easier for this positive density fluctuation to occur [87] (Figure 7.12).

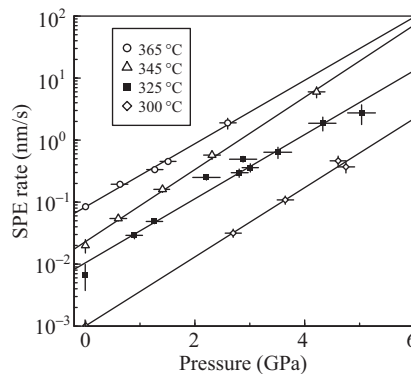


FIGURE 7.11 Solid-phase epitaxy (SPE) rate versus hydrostatic pressure for germanium (001). The activation volume was determined to be $\Delta V^* = -0.43 \Omega_{\text{Ge}}$. After Ref. [85].

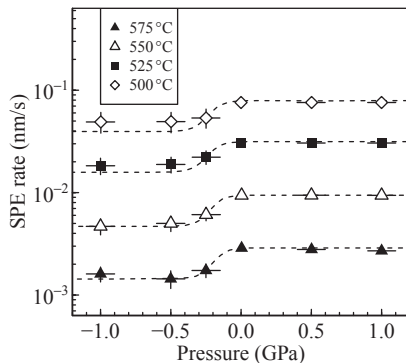


FIGURE 7.12 Solid-phase epitaxy (SPE) versus uniaxial strain in the plane of growth, σ_{11} , in silicon (100). Dashed lines are fits. After Ref. [91].

7.3.4.2 Nonhydrostatic Stress

Nonhydrostatic stress effects have been imposed by methods such as the elastic bending of wafers or the clamping of wafers face-to-face while inserting them in a furnace for SPE. These stress states are essentially homogeneous spatially, and their effects on the velocity of a planar interface have been characterized. The understanding of the influence of homogeneous, nonhydrostatic stress states on unidirectional SPE is anticipated to be necessary, but not sufficient, for the understanding and control of the effects of inhomogeneous, nonhydrostatic stress states on multidirectional SPE during device fabrication.

The original experiments of Aziz et al. [67] on the effect of nonhydrostatic stress on the SPE rate spanned tensile and compressive uniaxial stresses of magnitude up to approximately 0.6 GPa. They found that uniaxial in-plane tension raised v whereas uniaxial in-plane compression reduced v . In contrast, uniaxial compression normal to the plane of the interface raised v [88]. This behavior was interpreted by assuming that v is limited by a single thermally activated process, and extending transition state theory to nonhydrostatic stress states. The result is

$$v(\sigma) = v(0)\exp\left(\sigma_{ij}\Delta V_{ij}^*/kT\right), \quad (7.11)$$

where the sum over repeated indices $i, j = 1, 2, 3$ is implied. The activation volume, which characterizes the kinetic response to hydrostatic pressure, becomes generalized to the activation strain tensor, characterizing the kinetic response to nonhydrostatic stress [67]. The combined measurements on Si(001) are characterized by a tensor of the form

$$\Delta V_{ij}^* = \begin{pmatrix} 0.15 & 0 & 0 \\ 0 & 0.15 & 0 \\ 0 & 0 & -0.58 \end{pmatrix} \Omega \quad (7.12)$$

indicating an average transition state of tetragonal symmetry exhibiting in-plane dilation along with contraction in the direction normal to the interface [69].

More recent experiments by Rudawski et al. [89] spanned stresses of magnitude up to 1.5 GPa. In contrast to the prior results on Si(001), they found negligible enhancement by uniaxial in-plane tension, but a rapid retardation with uniaxial in-plane compression, approaching saturation at approximately -0.5 GPa. An example of these trends is shown in Fig. 7.12. The discrepancies between these and the prior results have not been fully resolved.

Rudawski et al. have advanced various explanations of their observed behavior, but they all involve the mechanism of 2D monolayer island nucleation and lateral growth. In the classic theory of 2D nucleation-limited growth, in the regime where many 2D nuclei exist simultaneously on a surface, the overall growth rate is described by $v \propto (I \times v_1 \times v_2)^{1/3}$, where I is the 2D nucleation rate, v_1 is the ledge speed in one principal in-plane direction, and v_2 is the ledge speed in the other principal in-plane direction [90]. If each of these three processes is a simple thermally activated process, then $d \ln v / dX$ —where X represents a thermodynamic property such as $(1/kT)$, P , or σ_{ij} —is simply the arithmetic mean of the corresponding properties of I , v_1 , and v_2 . In this case, the behavior of v phenomenologically would appear to be that of a single, thermally activated process with unique activation energy, volume, and strain. This is inconsistent with the experimental results of Rudawski et al.

To account for their observed, more complex SPE stress-dependence, Rudawski et al. assumed there is a lag time for 2D nucleation. This creates a more complex relationship between v and the rates of 2D nucleation and lateral island growth, so that v no longer must appear to be characterized phenomenologically by a single, thermally activated process. The most recent version of their model fits their data for the uniaxial stress-dependence quite well over the range -1.0 to 1.0 GPa for 500°C , 525°C , 550°C , and 575°C , but data at each temperature were fitted independently without attempting to fit the temperature dependence itself [91].

If this model is correct, it should also lead to a temperature dependence that cannot be characterized by a unique activation energy, which should show up in the temperature-dependence data, at some level of accuracy to be determined by evaluating the predictions of the model. It has been pointed out that the temperature-dependence data of Olson and Roth, spanning about 10 orders of magnitude in v in stress-free material, can be fitted by a model of two thermally activated processes occurring in series, as long as the activation energies of those processes differ by less than approximately 0.5 eV [69]. Recognizing that it could be difficult experimentally to span a large temperature range while under stress, it may be interesting to examine the temperature dependence at compressive stresses such as 0 to -0.3 GPa, where the stress dependence is so unusual that the temperature dependence may be nontrivial.

Recent MD simulations of Si(001) SPE using the Tersoff 3 potential at 1700 K reproduce qualitatively the enhancement by hydrostatic pressure, the retardation by uniaxial in-plane compression, and the small or nonexistent effect of uniaxial in-plane tension [92]. These simulations overestimate v by about an order of magnitude, but

reproduce the experimental activation energy within 0.05 eV; they overestimate the experimental activation volume by about a factor of three and underestimate the retardation effect of in-plane uniaxial compression by about the same factor. Unfortunately, the details of interface structure and atomic trajectories have not yet been examined for any direct evidence of 2D nucleation and lateral growth. In fact, although lateral terrace growth has been identified in MD of Si(111) SPE [93], the 2D nucleation and lateral growth mechanism has not been identified in any MD simulation for Si(001)—even one in which the interface structure or atomic trajectories are carefully scrutinized, such as in [93] or [94].

An alternative hypothesis for the apparent discontinuity in slope at the origin of the Si(001) SPE rate versus uniaxial in-plane stress is that there is a degeneracy in transition states at the stress-free configuration, and this degeneracy is broken by the application of stress, leading to different transition state configurations in compression and tension. These ideas have been discussed for bulk atomic diffusion in c-Si [95,96].

Rudawski et al. [97] have extended their studies to the effects of inhomogeneous nonhydrostatic stresses on multidirectional SPE in device fabrication geometries. Important additional effects arise during multidirectional SPE that are beyond the ability to extrapolate from homogeneous stress effects in unidirectional SPE, and include *c*–*a* interface pinning by surfaces, high interface curvature effects, and the formation of mask-edge extended defects.

7.3.4.3 Interface Roughening

In-plane compressive stress in SPE has been shown to lead to the morphological instability of a planar Si(001) growth front, whereas tensile stress has a stabilizing effect [98,99]. Consequently, the *c*–*a* interface under compression becomes rough on lateral length scales of tens to hundreds of nanometers during SPE. Both compression and tension have been observed to result in the formation of crystallographic defects in the as-grown layer [89].

Barvosa-Carter et al. [29,98,99] accounted for these observations with a kinetically driven interfacial instability model. In this model, stress relaxation in the amorphous phase means that a sinusoidal perturbation to the interface morphology results in stress concentrations in the troughs, and stress relaxation at the peaks, of the morphology of the growing crystal. The troughs are thus slowed further under compressive stress, and accelerated further under tensile stress, leading to instability and stability, respectively. This effect has been used to stabilize heteroepitaxial growth of Si–Ge alloys on Si using tensile strain, under conditions that would lead to interfacial breakdown in the absence of strain [100].

Morarka et al. [101] have argued that the magnitude of the stress concentration is insufficient to account quantitatively for the observations, and have advanced a model in which the applied stress is hypothesized to modify the interfacial tension. They have been able to obtain good agreement with morphologies they observe in multidirectional SPE in device fabrication geometries.

7.3.5 Ion Beam-Induced Epitaxial Crystallization

Ion beam irradiation causes amorphization in Si and Ge provided that the fluence and ion mass is great enough and the substrate temperature is not too high. If an *a*-Si sample containing a buried *c*-*a* interface is irradiated while held at temperatures greater than 150 °C, there is competition between amorphization and recrystallization. This particular recrystallization is not only a result of the temperature, but also of a complex mechanism involving the formation of nucleation sites for nonequilibrium SPE growth (110) ledges at the *c*-*a* interface [102]. This process is referred to as *ion beam-induced epitaxial crystallization* (IBIEC).

The growth rate during IBIEC depends on the ion species, energy, ion fluence, and flux. Figure 7.13 shows the SPE growth rate for Si samples under Si, Ge, or gold (Au) irradiation at ion energies of 3 MeV with a flux of $2 \times 10^{12}/\text{cm}^2/\text{s}$. The growth rate is normalized to the number of displacements. The activation energies are much smaller than those required for pure thermal SPE regrowth so that crystallization can take place at temperatures as low as 200 °C. This may be advantageous for various applications requiring a low processing temperature and limited thermal budget. An ion mass effect is observed, so that it appears there is not a single activation energy that characterizes IBIEC, but one that is determined by the energy deposited in elastic collisions near the interface and also by the nature of the collision cascades formed by the injected ion [103].

As with thermal SPE, the *c*-*a* interface velocity under ion irradiation is affected by the substrate temperature, the presence of dopants, impurities, and crystal orientation [104]. The general similarity of thermal SPE and IBIEC behavior indicates that both processes are based on a similar atomic mechanism. Thermal SPE involves the nucleation and propagation of bond-breaking defects at the interface. It is possible

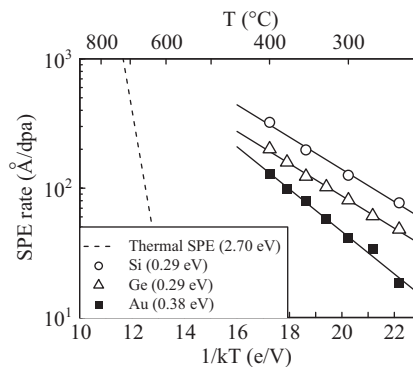


FIGURE 7.13 The ion beam-induced epitaxial crystallization regrowth rate normalized to the number of displacements for 3 MeV silicon (Si), germanium (Ge), and gold (Au) with a dose rate of $2 \times 10^{12}/\text{cm}^2/\text{s}$. The thermally induced solid-phase epitaxy (SPE) rates are also shown (dashed line). After Ref. [103].

that defects generated by the ion beam are converted to these particular defects at the c - a interface. Various defects have been proposed, including vacancies [105–107] and dangling bonds [108]. Given that the activation energy varies, more than one defect may be involved [103]. This has led to the phenomenological model proposed by Priolo et al. [102], which combines this idea of beam-generated defects with the kink motion model for SPE described in Figure 7.8. Here, the ion beam forms a dangling bond at a site on a {111} terrace of the interface. This process has been modeled using MC simulations to some success [75,109]. A detailed review of these calculations appears in [110].

7.3.6 Dopant Dependence

The SPE rate is enhanced or retarded markedly in the presence of impurity atoms. Csepregi et al. [3,112] found that group III and group V elements tend to enhance the SPE rate for concentrations greater than $10^{19}/\text{cm}^3$. Nondoping impurities, such as H, generally retard the interface motion. Enhancements of up to 30 times have been observed for B at impurity concentrations of 0.4 at.% [113]. Figure 7.14 illustrates the effect. In this example, a surface a -Si layer is implanted with arsenic (As) or aluminum (Al), or partially overlapping As and Al profiles, and annealed at 615 °C. During the initial stages of the anneal, the intrinsic SPE rate is observed. When the c - a interface meets the dopant-implanted region, its velocity increases and follows the concentration profile of the implanted dopant. The retardation in the near-surface region is the

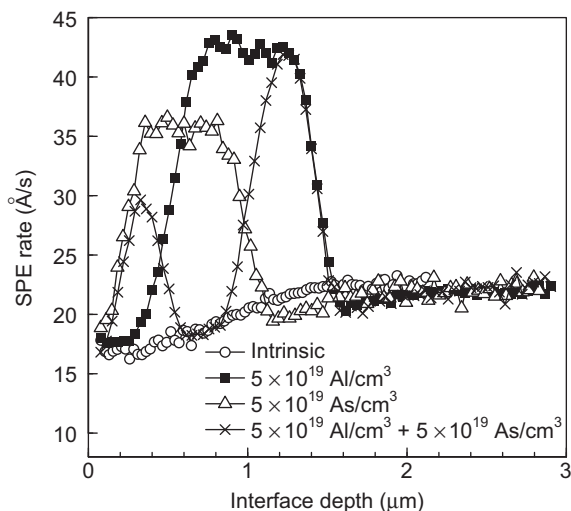


FIGURE 7.14 Solid-phase epitaxy (SPE) rate as a function of interface depth in samples doped with arsenic (As), aluminum (Al) and As + Al profiles implanted at multiple energies to create a constant concentration profile. The rates in an undoped sample are shown for comparison. Data from Ref. [111].

result of H infiltration (discussed further in Section 7.6.2). When both n- and p-type dopants are present in equal concentrations, the SPE rate returns to its intrinsic value. Likewise, the overlapping of two dopants of the same type gives an additive effect on the SPE regrowth rate [114]. These electronic effects suggest that the SPE rate is sensitive to shifts in the Fermi level and that both neutral and charged defects may be responsible for the SPE process. A number of models that link the structural and electrical properties at the c - a interface have been developed in an attempt to describe this phenomenon [114–120].

The charged kink site model proposed by Williams and Elliman in particular has been instrumental in the development of our current understanding of dopant effects on SPE. The model considers a bond-breaking process that propagates along [110] ledges, as depicted in Figure 7.8 [116,121]. It is assumed that the growth sites have electronic energy levels inside the band gap, thus linking the atomic structure at the interface to shifts in the Fermi level. The kink site of this model can be visualized as some bond-breaking defect that is in thermal and electronic equilibrium, and is determined by the band structure and density of states of the crystal. The SPE velocity of the interface in an n -type doped and intrinsic material is expected to be proportional to the concentration of these defects, and can be written as

$$v = A([D^0] + [D^-]_d) \quad (7.13a)$$

and

$$v_i = A([D^0][D^-]_i) \quad (7.13b)$$

respectively, where A is a constant at a given temperature and $[D^0]$ is the concentration of uncharged kink sites and is independent of doping. $[D^-]_d$ and $[D^-]_i$ are the concentrations of charged kink sites in the doped and intrinsic material, respectively. These equations assume that SPE is dominated by D^0 and D^- , and that each of these defects is equally capable of promoting interface motion. The charged fraction of defects is determined by Fermi–Dirac statistics and is expressed as the ratio of charged to neutral defect concentrations in the crystal,

$$\frac{[D^-]_{\text{doped}}}{[D^0]} = g \exp\left(\frac{E_f - E^-}{kT}\right) \quad (7.14)$$

where E_f is the Fermi level and E^- represents the energy level within the band gap associated with the SPE defect. It is assumed that the negatively charged defect energy level tracks the conduction band edge, E_c . The degeneracy factor, g , associated with E^- is given by $g = Z(D^-)/Z(D^0)$, where $Z(D^-)$ and $Z(D^0)$ are the internal degeneracies of the D^- and D^0 defect states, respectively [122]. If a dangling bond defect is responsible for the SPE process, then it is expected that $Z(D^0) = 2$ because one electron of either spin can be added to make a neutral bond. $Z(D^-)$ will equal unity because there is already an electron at the site, so there is only one choice for the spin of the additional electron. Therefore, $g = 1/2$ only if the spin degeneracy needs to be

considered. For the positive charge state, $g = 1$ as the degeneracy of the valence band also contributes a factor of two. Substituting Eqn (7.14) into Eqn (7.13) gives

$$\frac{v}{v_i} = \frac{1 + \left. \frac{[D^-]}{[D^0]} \right|_{\text{doped}}}{1 + \left. \frac{[D^-]}{[D^0]} \right|_{\text{intrinsic}}} = \frac{1 + g \exp\left(\frac{E_f - E^-}{kT}\right)}{1 + g \exp\left(\frac{E_{fi} - E^-}{kT}\right)}. \quad (7.15)$$

This generalized Fermi-level shifting (GFLS) model can be used to fit the normalized SPE data as a function of temperature with the degeneracy, g , and the energy level, E^- , of the SPE defect being free parameters [71,113,123,124]. Lu et al [85] assumed that the mobilities of charged and uncharged DBs are identical. If the charged and neutral defect concentrations are weighted separately with a factor A and A' in Eqn (7.9), then this has the effect of weighting the degeneracy factor in Eqn (7.15) by a value of A'/A . The energy level of the defect predicted by the model will be unaffected by this assumption.

A shortcoming of the model is that the temperature dependence of this energy level is not known and cannot be included in these calculations, as pointed out by Lu et al. [52]. However, a detailed account of the model and its application to an extensive data set should provide much insight into the nature of the SPE process. Two parameters that must be calculated to apply Eqn (7.15) to normalized SPE data are E_{fi} and E_f , the Fermi level of an intrinsic and doped semiconductor, respectively.

Figure 7.15(a) shows the Fermi level as a function of As concentration in Si calculated using both extrinsic and degenerate semiconductor statistics. In the degenerate case, the charge neutrality equation is solved numerically for the Fermi level. In the dopant concentration range where SPE enhancements are observed ($\sim 1 \times 10^{19}/\text{cm}^3$), the extrinsic and degenerate Fermi levels diverge. The degenerate case appears to be a more realistic derivation for the case when the material is highly doped [123,124].

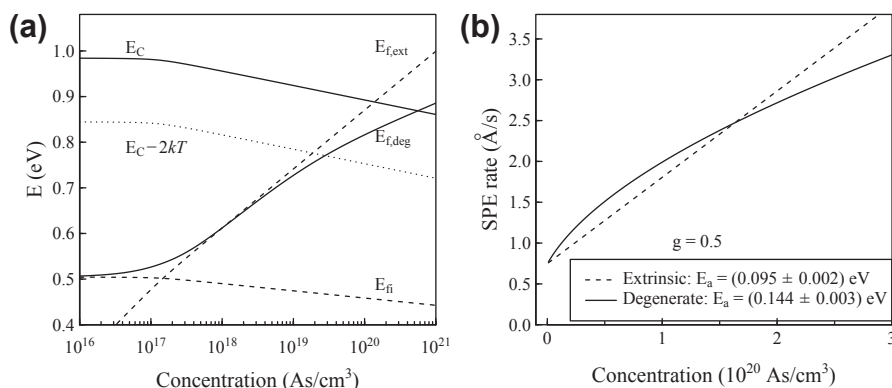


FIGURE 7.15 (a) The Fermi level at 537 °C as a function of arsenic (As) concentration calculated by solving the electrical neutrality condition for a degenerate semiconductor. The dashed line represents the Fermi level calculated using nondegenerate semiconductor statistics. The dotted line represents a $2kT$ window beyond which the extrinsic and degenerate approaches diverge. (b) The predicted solid-phase epitaxy (SPE) rate calculated from the extrinsic and degenerate Fermi levels, with the degeneracy of the SPE defect fixed at 0.5.

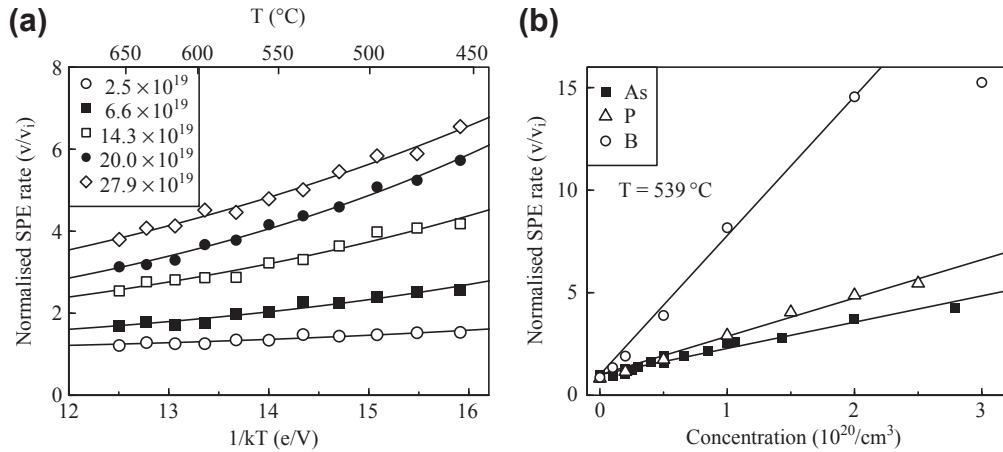


FIGURE 7.16 (a, b) The solid-phase epitaxy (SPE) rate of arsenic (As)-implanted silicon (Si) as a function of inverse temperature (a) and as a function of dopant concentration (b) both normalized by the intrinsic SPE rate. SPE rates for boron (b) and phosphorus (P) are also shown for comparison in (b). The SPE rates from the samples with the highest B concentration were excluded from the fits. Solid lines are fits using Eqn (7.15) with both g and E_a as free parameters, and the Fermi level calculated with an extrinsic model.

For the purposes of developing a phenomenological model with the greatest predictive power, both degenerate and extrinsic cases have been considered. When these Fermi levels are integrated into Eqn (7.15), it can be seen that they predict different SPE rate dependences on the dopant concentration (Figure 7.15(b)). The extrinsic model results in a linear dependence whereas the degenerate model predicts a nonlinear trend.

Figure 7.16 shows the As SPE rates as a function of both inverse anneal temperature (Figure 7.16(a)) and dopant concentration (Figure 7.16(b)). First, it should be noted that both degenerate and extrinsic models fit the data excellently in Figure 7.16(a) as long as g and E_a are allowed to vary for each data set. In Figure 7.16(b), the normalized SPE rate is observed to be approximately linear, with dopant concentration consistent with previous results [119,125]. However, a discrepancy between the different dopants is clear. The difference in ionization energies of As and P cannot account for this discrepancy. These trends suggest that another effect is not captured appropriately by the model.

7.3.6.1 Dopant-Induced Strain

In an alternative treatment, the trends observed in Figure 7.15 have been attributed to dopant-induced stress [126–128]. The stress arising from the incorporation of a high concentration of dopant atoms that differ in size from the host lattice atoms can be obtained from Vegard's law,

$$\varepsilon_{||} = \frac{a - a'}{a} \quad (7.16)$$

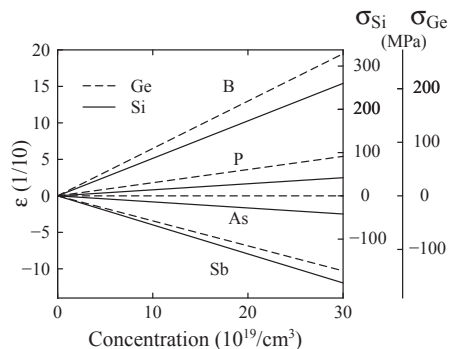


FIGURE 7.17 Strain dependence on dopant concentration in silicon (Si; solid lines) and germanium (Ge; dashed lines) for various common dopants. Young's modulus in the (110) direction was taken to be 168.7 GPa and 136.2 GPa for Si and Ge, respectively [130]. As, arsenic; B, boron; P, phosphorus; Sb, antimony.

where a is 5.431 and 5.66 Å for Si and Ge, respectively. The lattice parameter of the layer containing the dopant is $a' = a(1 - C_D) + a_D C_D$, where C_D is the atomic fraction of the dopant in the sample. The lattice parameter of the dopant, a_D , is determined using the covalent radii [129]. In the direction of growth, there is no stress because the lattice parameter can expand or contract as a result of the plasticity of the amorphous overlayer.

Figure 7.17 shows the strain in the plane of SPE growth introduced into Si or Ge lattice as a function of the concentration for several different dopants determined with Eqn (7.16). The strain, σ , on the right axis is related to the stress via Young's modulus (Hooke's law). These strains are relatively small compared with those present in uniaxial strain measurements [131].

Interestingly, the trends in Figure 7.16 suggest that dopants causing a tensile strain enhance the SPE rate whereas those resulting in a compressive strain retard the SPE rate as described by Eqn (7.11). To capture this trend, we start with an expression of the form

$$\frac{v}{v_i} = \left(1 + \frac{N_d}{N_C} e^{(E_c - E^-)/kT}\right) \exp(\sigma_{\parallel} \Delta V_{\parallel} / kT) \quad (7.17)$$

assuming that stress and Fermi-level shifting effects are separable [132]. Figure 7.18 shows As- and P-enhanced SPE data in Si. The dopant concentrations are normalized by Eqn (7.17), so that for a good fit the data should fall along the $y = x$ line. For the greatest P concentrations ($> 2 \times 10^{20}/\text{cm}^3$), the SPE rate is overestimated. This may be a result of incomplete dopant activation resulting from dopant clustering at these high concentrations. In p-type Si, a similar deviation is observed for B concentrations more than $1.5 \times 10^{20}/\text{cm}^3$, which is in agreement with earlier measurements [133].

For a global fit for both P and As data sets, $E_c - E^- = 0.118$ eV and $\Delta V = 5 \Omega_{\text{Si}}$ were obtained with the degeneracy again fixed at $g = 0.5$. This energy level is similar to that found in previous works [113,126,127]. However, the activation volume is much greater than that found for intrinsic Si in uniaxial stress measurements ($0.15 \Omega_{\text{Si}}$) [67], as

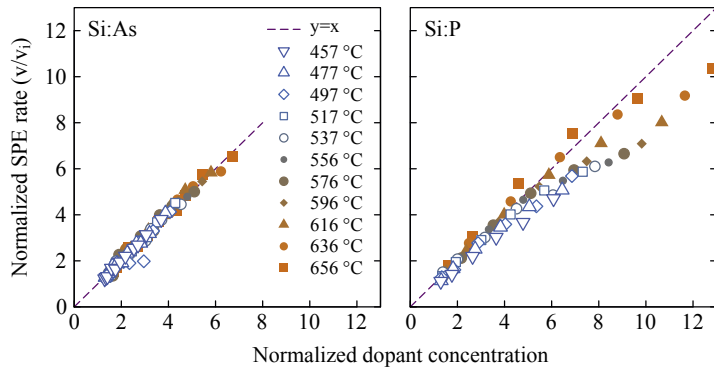


FIGURE 7.18 The normalized solid-phase epitaxy (SPE) rate for arsenic- (As) and phosphorus (P)-implanted amorphous-silicon (Si) layers (from Refs [113,124]) for various anneal temperatures as a function of the normalized dopant concentration. The dopant concentration, N_{dr} is normalized by Eqn (7.17) with $(E_c - E^-) = (0.118 \pm 0.009)$ eV, $g = 0.5$, and $\Delta V(5 \pm 2)$ Ω .

Table 7.1 Summary of the SPE Defect Energy Level and Degeneracy, and the Activation Volume in a Doped Semiconductor Determined with the Extrinsic GFLS Model (Eqn (7.17))

	ΔE (eV)	g	ΔV_{\parallel}
n-Type Si	0.118 ± 0.009	0.5	$(5 \pm 2) \Omega_{Si}$
p-Type Si	0.149 ± 0.009	1	$(3.5 \pm 2) \Omega_{Si}$
n-Type Ge	0.007 ± 0.002	0.5	$(3 \pm 2) \Omega_{Ge}$

Errors are from the fits only.

observed previously. Dopant-enhanced SPE clearly depends on dopant-induced stress because relative stress values are consistent with the difference in enhanced SPE rates between different dopants of the same type. However, other effects, including band bending at the interface and stress-induced changes in the band structure, may also play a role. The results are summarized in Table 7.1 [126,127].

7.3.7 Dopant Activation

The dopant solubility limit is the maximum concentration that can be achieved in equilibrium with its host lattice, and it is determined by the thermodynamic requirement that the free energy of the system be minimized. Various factors are involved in achieving this, including atom size and crystal structure. In general, active concentrations well above the solubility limit are possible using SPE. For example, concentrations of $9 \times 10^{21}/\text{cm}^3$ active As have been reported in Si [134], whereas the equilibrium concentration is $1.5 \times 10^{21}/\text{cm}^3$ [135]. The exact value is strongly dependent on the experimental conditions. Values for both Si and Ge are shown in Figure 7.19.

For front-end CMOS processing, the electrical activation of implanted dopants after an SPE anneal is a critical parameter and has thus been studied in some detail

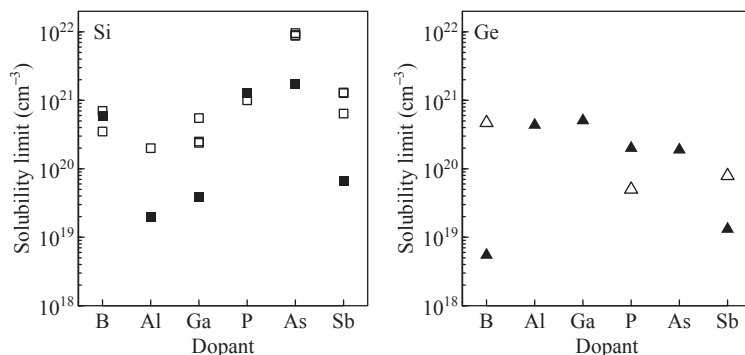


FIGURE 7.19 Maximum equilibrium solid solubility (closed symbols) [135] and metastable solid solubility after solid-phase epitaxy (SPE) (open symbols) of common dopants in silicon (Si) and germanium (Ge). Al, aluminum; As, arsenic; B, boron; Sb, antimony. Data from Refs [128,136–140].

[7,141–144]. The activated dopant concentration is dependent on the parameters of the anneal. For example, the sheet resistance for BF_2 implanted samples is reduced for both a higher anneal temperature and a higher anneal ramp rate [141].

The thermal stability of an activated dopant profile is also a critical parameter for which subsequent high-temperature processing may be a necessary component of the device process flow after the SPE anneal (e.g., silicide formation). Dopant deactivation can occur, increasing the sheet resistance, at temperatures greater than the SPE anneal temperature. A so-called “reverse annealing” effect is often observed for anneals at higher temperatures [145,146]. However, the behavior may be dominated by longer range redistribution of the dopants rather than an actual reactivation of the dopant. Variations in sheet resistance can be driven by dopant deactivation via the release of interstitials from end-of-range defects [142] or dopant clustering, as discussed further in Section 7.6. Hence, detailed characterization is often required to optimize dopant profiles.

7.4 Atomistic Models

Although the kinetic models discussed in the previous section can predict the SPE regrowth rate accurately in a wide range of experimental conditions, they provide little insight into the atomic rearrangements at the c - a interface. Atomistic models have been developed that provide plausible mechanisms, starting with a structural model of the c - a interface by Spaepen [58] and Spaepen and Turnbull [59], in which a bond-breaking mechanism at the interface is operative. Saito and Ohdomari [147] developed this model further by using a modified Keating potential (harmonic springs in bond angle and bond length) to evaluate the distortion energy associated with bond rearrangements. More recent research using MC and MD methods have refined our understanding further.

7.4.1 Construction of Materials

To model the SPE process atomistically, the crystalline and amorphous phases must be constructed, and so must an interface separating them. The structures of these were discussed briefly in [Section 7.3.1](#). The very first amorphous models were based on the CRN and were made by hand, as reported by Polk in 1971 [\[148\]](#). To overcome issues with bias and free surfaces, numerical MC methods were developed, such as the Wooten, Winer, and Weaire (WWW) method [\[40\]](#). With this method, bonds are switched in a crystalline lattice to introduce five- and sevenfold rings. The structure is then relaxed by using a harmonic Keating potential. More recently, amorphous tetrahedrally bonded semiconductors have been constructed by reverse-MC methods, in which a structure is optimized using experimental data input constraints rather than by minimizing the bond energy [\[47,149,150\]](#). With these methods, a coordination change, such as in WWW, is made at random. The change is accepted if it improves the fit to the data, but if the fit becomes worse, it is rejected with a probability that depends on how much it makes the fit worse. The c - a interface may be constructed, with no dangling bonds, by confining the MC bond-switching events to a half space within the crystal.

MD methods have also been used to construct an a - c interface. One approach has been by simulating ion implantation [\[151\]](#); another has been by simulating rapid temperature quenching from the melt. In melt quenching using some interatomic potentials, an intermediate, supercooled liquid phase with high coordination number, distinct from the tetrahedral amorphous structure, can result [\[152–155\]](#). In such cases, modifications to the potential, or additional processing steps, are required to obtain a structure representative of the amorphous semiconducting phase.

7.4.2 Monte Carlo Simulations of Solid-Phase Epitaxy

MC simulations are commonly used to address longer timescales and larger atom numbers than can be computed practically using MD. They consider only part of the system, such as the c - a interface or defect evolution, and neglect vibrations about metastable equilibrium positions. Changes in configuration occur on much longer timescales than atomic vibrations. Thus, larger samples and longer time frames can be considered, meaning a broader range of experimental parameters may be explored.

In IBIEC ([Section 7.3.5](#)) investigations, MC simulations have been used to study the evolution of the c - a interface [\[75\]](#). Instead of a crystallization event occurring at kink sites along $[110]$ ledges, dangling bonds nucleate anywhere on a $\{111\}$ terrace of the interface. The probability of this dangling bond causing a crystallization event then depends on its immediate environment (i.e., the probability is greater when there are more atoms that are a part of the crystalline phase in the vicinity). This process enhances the interface roughness as the interface moves through the amorphous phase, and affects the interface velocity, making the crystal orientation dependence distinct from that observed for thermal SPE [\[109,110\]](#). Such MC simulations are in excellent agreement with experiments.

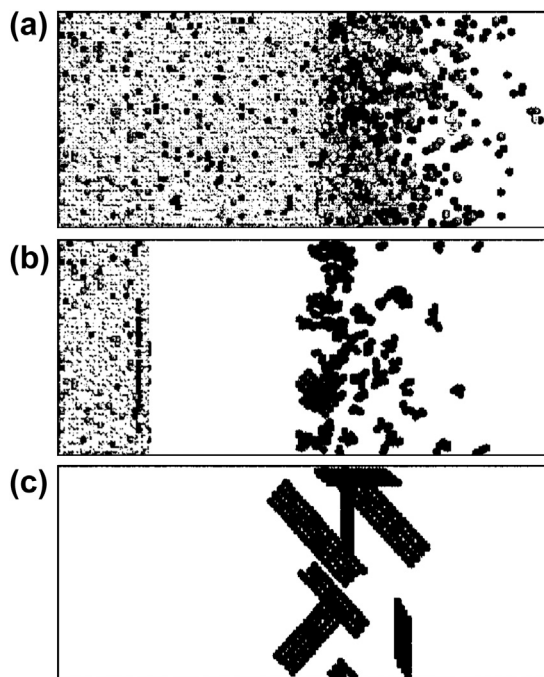


FIGURE 7.20 (a–c) The evolution of defects in a nonlattice kinetic Monte Carlo simulation of silicon (Si) implanted with 5 keV Si (a) followed by an anneal at 500 °C (b) and 800 °C (c). Reprinted with permission from Ref. [33]. Copyright 2004, AIP Publishing LLC.

MC methods have also been used to model thermally activated SPE. Pelaz et al. have studied the evolution of residual implantation damage during SPE regrowth using nonlattice MC simulations [33,156]. In their model, only the defects created by amorphizing implants are considered, and their positions do not necessarily correspond to actual lattice locations. These defects consist of interstitial–vacancy pairs and, in this model, may make up the amorphous layer. Figure 7.20(a) shows a continuous amorphous Si layer on the left in contact with a crystalline substrate. The c – a interface is not sharply defined, as defects appear on the crystal side of the interface. On annealing, the recombination rate of interstitial–vacancy pairs is given a dependence on the number of neighboring pairs. Consequently, pairs are most likely to recombine when the number of neighboring pairs is small, such as at the c – a interface. Excess self-interstitials and vacancies remain in the vicinity of the original c – a interface. These defects evolve into more complex defects such as $\{311\}$ defects or dislocation loops (Figure 7.20(C)). At greater temperatures, interstitials may be released from such defects, causing transient enhanced diffusion of dopants in the near-surface region.

When the crystal lattice is included, such as in lattice kinetic MC, other parameters can be explored, such as the orientation dependence, stress dependence, and anisotropic growth behavior in Si(111) SPE [74,157–159]. In these models, a more realistic SPE

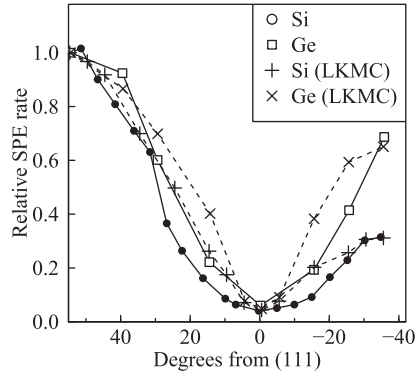


FIGURE 7.21 Normalized solid-phase epitaxy (SPE) rate versus the substrate orientation angle relative to the (111) direction. Silicon (Si) data (550 °C) from Ref. [72] and germanium (Ge) data (330 °C) from Ref. [74]. lattice kinetic MC simulation results from Refs [74,157].

mechanism can be investigated in which, as with the early atomistic models, an atom within the amorphous phase is required to form at least two bonds with the crystal phase to become part of that crystal phase. The orientation dependence is modeled by using three different preexponential factors for growth on (100), (110), and (111) interfaces. Figure 7.21 shows the orientation dependence for both Si and Ge extracted from both experimental data and simulations. In a detailed analysis of the simulated SPE on Si(110) and (111) substrates, pathways for the formation of twin-type defects are demonstrated. Early stages of SPE are characterized by the formation of defects. An increased interface roughness in the later stages of SPE arising from twin-defect formation enhances the SPE growth rate via SPE events on (100) sites consistent with experimental observation.

7.4.3 Molecular Dynamics Simulations of Solid-Phase Epitaxy

MD simulations describe processes and reactions on the atomic scale, thereby providing atomic-level insight. However, a typical time step in MD is 1 fs because the vibrational movement of every atom in a sample is tracked. The resulting number of time steps is so large that the calculational simplicity of classic interatomic potentials has been required—except, occasionally, for the very last time steps before equilibration [61]. The number of atoms and the timescales that can be simulated tend to be limited to less than about 10^6 atoms and 1 ns, respectively. In a typical MD simulation of SPE, an amorphous material is prepared in a cell consisting of hundreds to thousands of atoms. The generation of the amorphous region by MD techniques was discussed in Section 7.4.1. Only part of the cell is amorphized, leaving an interface between the amorphous phase and a crystalline seed. During MD simulations, the time evolution of the c - a interface is followed and the growth velocity can be extracted by, say, keeping a count of the number of atoms satisfying certain criteria. Figure 7.22 shows results from a typical SPE MD simulation, illustrating crystallization reminiscent of that observed experimentally, as presented in Figure 7.1 at the start of this chapter.

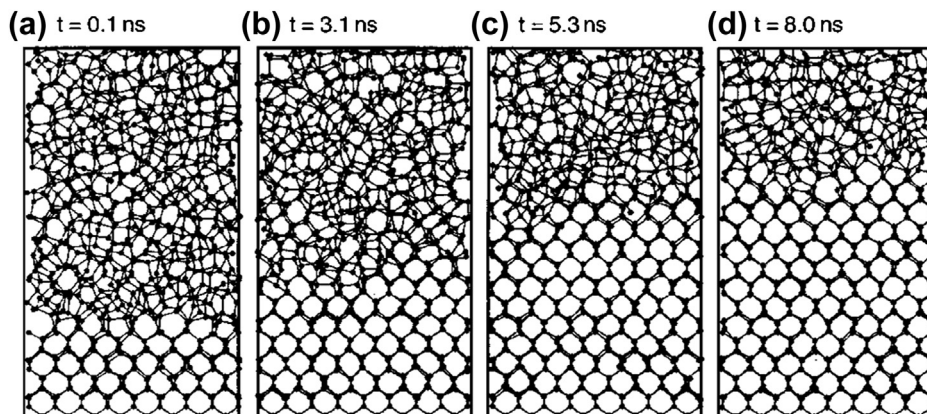


FIGURE 7.22 (a–d) Typical molecular dynamics (MD) simulation results of solid-phase epitaxy (SPE) growth. The MD cell is annealed at 1800 K and changes in the atomic coordinates annealed after 0.1 ns (a), 3.1 ns (b), 5.3 ns (c), and 8.0 ns (d) are shown. From Ref. [160].

The interatomic potential governs the interactions between atoms in the solid and must account accurately for the stability of the diamond cubic structure, along with its elastic moduli and vibrational properties. To be useful in modeling SPE, it should also match the properties of the amorphous phase, such as the latent heat of crystallization and the tetrahedral coordination. The Stillinger-Weber (SW) potential was one of the first potentials used to describe diamond lattices [161]. This potential remains popular for its simplicity and relatively realistic description of the crystal phase [154,162–166]. It introduces directional bonding through an explicit three-body term. This also gives rise to its poor transferability—that is, it cannot be used reliably to study properties other than those for which it is optimized. A variety of other potentials have been developed to address this issue, such as the Tersoff 3 parameterization potential [160,163,167,168], and the environment-dependent interatomic potential (EDIP) [94]. A reparameterized SW (SW115) [169] and Lenosky modified embedded atom method [163,170] have also been useful.

Although the computation time is limited in an MD simulation, the influence of a wide range of experimental situations has been explored, including the dependence of the SPE rate on temperature [163], interface orientation [92,93], pressure [92,94,171,172], stress [92,94], SPE in confined regions [173,174], and B segregation and precipitation during SPE [175].

Figure 7.23 is an Arrhenius plot of the Si SPE rates extracted from MD simulations using several different potentials and compared with the experimental data characterized by an activation energy of 2.7 eV. The variations in SPE rate among different potentials is enormous. Presumably, the methods used to prepare the amorphous phase have a relatively small effect on the extracted SPE velocity compared with the effect of the potential chosen. Many of the potentials predict an SPE rate that, in contrast to the experimental data, does not exhibit Arrhenius behavior. The simulations exhibiting the

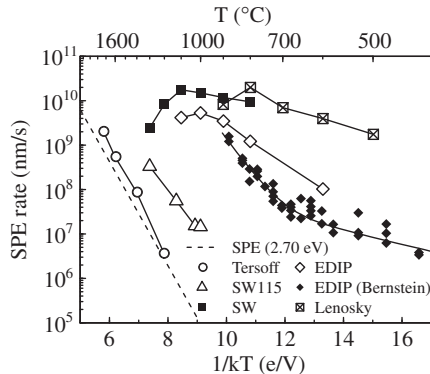


FIGURE 7.23 Solid-phase epitaxy (SPE) velocity as a function of inverse temperature for five different interatomic potentials and for experimental data (dashed line). SW, Stillinger-Weber. After Ref. [163].

greater velocities, on the order of 1 m/s, are likely to be modeling liquid-phase epitaxy [163]. This occurs, for example, in explosive crystallization during pulsed laser melting, when a metastable, undercooled metallic melt is formed at the c - a interface and the latent heat of crystallization of the liquid is more than the latent heat absorbed to melt the amorphous phase [176,177].

The potential most closely matching experiment in Figure 7.23 is the Tersoff 3, with an activation energy of 2.99 eV [178]. Comparing the simulated SPE rate and its dependence on externally imposed thermodynamic parameters with experimental values is one way to evaluate the quality of a potential, but it is not necessarily the ultimate arbiter of the credibility of a simulation. Indeed, it has been noted that although the Tersoff 3 interatomic potential reproduces the experimental SPE Arrhenius behavior well, it also predicts a melting point that is 50% greater than the experimental value [160,174]. Nevertheless, with judicious usage and systematic scrutiny, MD simulations provide improving insight into real processes.

After the simulation is judged adequate for reproducing macroscopic behavior, it may be used to investigate questions that are difficult (e.g., interface nanofacet morphology) or impossible (e.g., atomistic mechanistic pathway) to answer experimentally. Because these are behaviors for which the empirical potential is not fitted, we cannot be sure the outcome is realistic. Simulations gain credibility when several empirical potentials predict the same behavior (e.g., interface faceting) or when a behavior can be corroborated by experiment (e.g., a final polycrystalline configuration in fin-Field Effect Transistors (fin-FETs)).

We believe the following observations from MD simulations are noteworthy. MD simulations are providing insight into interface roughness versus interface orientation. For example, Lampin and Krzeminski [64,93] have examined interface configurations carefully. They observed that interface roughness is low on {001}, and higher on {011} and {111} because of the formation of nanoscale facets [179]. On {011}, they identified a growth mechanism in which the rate is limited by the formation and annihilation of

{111} nanofacets that appear to pin interface motion when they nucleate twins. For {111} interfaces, they identified a growth mechanism in which the rate is limited by {111} bilayer reordering associated with the formation of a twin-type defect. They found an increasing density of defects left behind in grown Si after SPE with {001}, {011}, and {111} surface orientations. They found a greater SPE rate before any defects formed than after. Last, they correlated their findings with the observation of Drosd and Washburn [180] that the completion of a sixfold ring in SPE at a {001}, {011}, and {111} plane requires that one, two, and three atoms, respectively, move into the correct position. In the latter case, with only short-range interatomic forces, it is equally easy for the three atoms to move into the positions that form a {111} twin.

The early results from Bernstein et al. [94] using the EDIP can be characterized by two activation energies on the low side: 0.4 eV at low temperatures and 2.0 eV at high temperatures. This behavior was attributed to the defect kinetics in their MD sample. Because fast quench times were used to prepare the sample, a high quenched-in defect concentration of a few atomic percent was present. At low temperatures, the migration barrier for these defects dominates, whereas at higher temperatures new defects are created thermally, thereby changing the slope on the Arrhenius plot.

Bernstein et al. [61,94] developed the means to identify possible atomistic mechanisms—collections of atomic trajectories—of SPE from their simulations. They identified mechanisms they called *simple* and others they called *complex*, within the same sample. An example of a more complex mechanism involves the migration of a fivefold coordinated defect to the interface, leading to the incorporation of two atoms into the crystal matrix. During migration, the defect alternates between a “floating bond” (overcoordination defect, fivefold) and a “dangling bond” (undercoordination defect, threefold). Such a mechanism is illustrated in Figure 7.24. The atomistic mechanism revealed from the simulations supports the Spaepen dangling bond migration model qualitatively [65]. It would be interesting to use the analysis techniques of Bernstein et al. to determine whether such mechanisms exist in today’s higher powered simulations.

7.5 Defects Formed during Solid-Phase Epitaxy

Defects have a profound effect on the operation of devices and the achievable limits in terms of downscaling. Usually, the crystal layer resulting from the SPE process is of a high quality. However, a band of dislocations at the original *c*–*a* interface (category II defects [181]) exists, commonly known as *end-of-range* (EOR) *defects*. During a low-temperature SPE anneal, these defects are found in the form of large interstitial clusters. As the annealing temperature is increased, {311} defects form, followed by various dislocation configurations. An anneal of 1000 °C for 24 hours is required to remove them completely. These defects were once thought to be inert, but it has come to light that they exchange point defects actively with their environment. Such defects drive transient enhanced diffusion of shallow dopant concentration profiles in Si. Making use of the strong bonding between Si interstitials and substitutional carbon (C), C implants can be

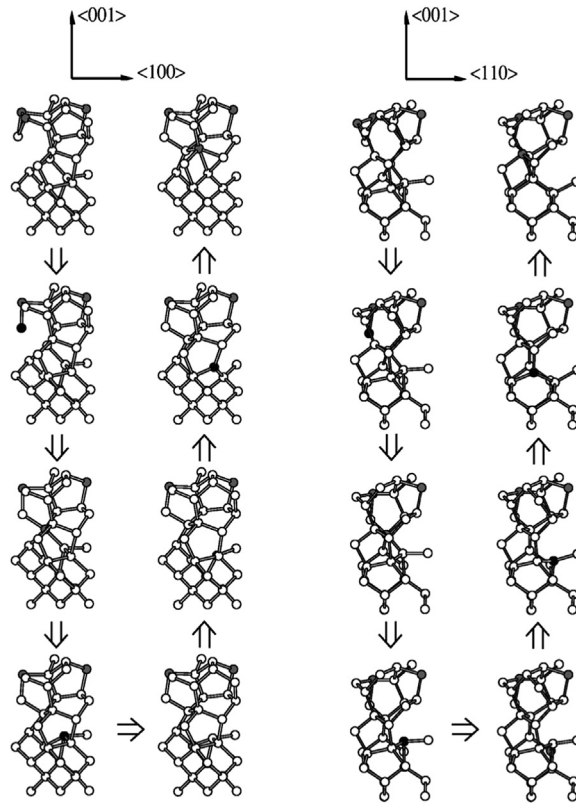


FIGURE 7.24 Illustration of a complex mechanism for crystallization. The sequence of steps is indicated by the arrows. Two views are shown for every step, along high-symmetry directions of the crystalline part, which is in the lower half of each image. Atoms with coordination other than four are shown shaded: black for threefold coordination and gray for fivefold coordination. Defect migration entails alternating between threefold and fivefold forms. From Ref. [94].

used to reduce the EOR defect density [182]. These EOR defects can be observed with TEM, electrical measurements (such as deep level transient spectroscopy), or photoluminescence, as shown in Figure 7.25.

SPE-induced defects are particularly prevalent after anneals of spatially confined amorphous regions, such as in finFETs and nanowires. SPE is dominated by both multidirectional regrowth and the proximity of free surfaces and amorphous/SiO₂ interfaces. The resulting defects are much more prominent in these samples, as exemplified in Figure 7.26 [183–185]. The high defect density would have an obvious impact on device performance and variability [186,187]. The shape of the initial amorphous region dominates the quality of the resulting crystalline material [188,189]. The crystal quality can be enhanced by aligning the *c*-*a* interfaces with major crystallographic directions [183].

A numerical technique based on level set theory has been used to understand the formation of trench or mask edge-type defects in 2D, and has been used to predict and

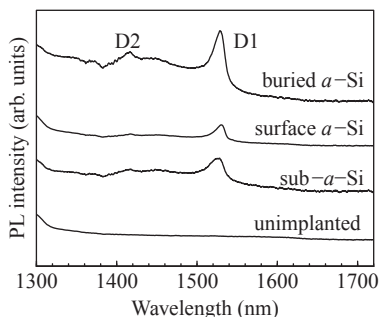


FIGURE 7.25 A 4.2-K photoluminescence spectra of buried, surface, and subamorphous (sub-*a*) layers on silicon (Si) (100) substrates annealed at 1000 °C in an oxygen ambient. The spectra are displaced vertically for clarity. The spectra from unimplanted Si are also shown for comparison. *a*, amorphous; arb., arbitrary.

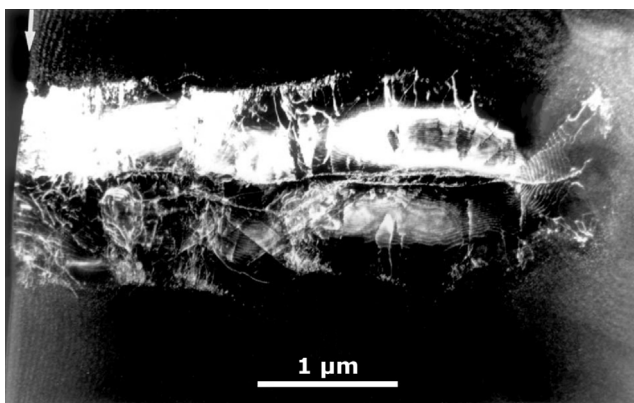


FIGURE 7.26 Weak-beam dark-field image of a deep amorphous well, annealed at 620 °C. The surface is to the left and the annealed amorphous well extends from the surface into the substrate to the right. The grain boundary dislocation arrays are particular evident in this image [183]. Reprinted from Ref. [183] with permission from Elsevier.

minimize the impact of these defects [21,23,190]. In the model, the amorphous region defines a shape in the x - y plane. This plane intersects a 3D shape that extends in the z direction. As this plane is moved up, the boundaries of the amorphous region change. In addition to orientation dependence, the c - a interface curvature also has a significant effect on SPE velocity.

If the orientation of the original crystal is (or close to) the $\langle 111 \rangle$ direction, or the dopant concentrations approach the solid solubility limit, the resulting crystal may also contain defects (category III and V defects, respectively). The latter case yields dislocations at the peak in the implanted dopant profile [5]. Twins have been observed for crystal growth on a $\langle 111 \rangle$ substrate that are a result of stacking faults [191]. Defects are also created when the two interfaces of a buried amorphous layer meet (category IV

defects). These defects are the result of the misalignment of the two crystal seeds before crystallization and the extra interstitials implanted into the amorphous layer.

SPE is not only sensitive to the impurity content of the amorphous layer, but also to structural inhomogeneities. It has been shown that nanocavities formed by high-fluence H or helium implantation into *c*-Si are unstable under further ion implantation [192]. Although cross-sectional TEM and Au gettering experiments showed no evidence of nanocavities after amorphization, the SPE rate exhibited a retardation as the *c*-*a* interface proceeded through the region where the nanocavities previously existed [193]. Although residual H at the depth of the original nanocavity band may play a role in SPE rate retardation, it is speculated that structural defects that are not otherwise easily detected also contribute. Similarly, SPE rate retardation has been observed in ultrahigh-dose Si ion implantation into *a*-Si [194]. There, the regrowth rate exhibited a slow-down within the high-dose implanted region, and the dependence of this on implant temperature suggested that structural defects that would result in retarded SPE were less abundant for higher temperature implants.

The combination of shrinking device dimensions and growing computing power is creating opportunities for more realistic MD simulations of defect formation in device fabrication. Lampin and Krzeminski [174] recently performed MD simulations of SPE in an atomistic model of an oxide-coated finFET with linear dimensions reaching one fourth of those in an actual device. The simulation accounted for many of the defect features observed experimentally, such as the initially perfect epitaxy followed by the development of twins during growth, leading to a final region of random nucleation and polycrystalline growth. A control “experiment” with periodic boundary conditions instead of oxide interfaces did not evolve these features. The real-time and atomistic nature of “observation” in MD permitted them to identify, for example, the initiation of twin defects at the Si–oxide interface.

7.6 Diffusion and Segregation of Impurities during Solid-Phase Epitaxy

7.6.1 Dopants

Many dopants undergo diffusion, form defect complexes, and precipitate during SPE. These are complex, interacting phenomena that will, however, only be treated briefly here, with only the most relevant references given for further reading. Dopant clustering leads to electrical deactivation and occurs when dopant atoms diffuse during the activation anneal. This deactivation can cause retardation of the SPE rate, as measured readily with TRR [5]. Obviously, for the semiconductor industry, dopant deactivation is a serious issue for the fabrication of devices and is typically minimized by using limited thermal budgets.

The impurity diffusion mechanism in the amorphous phase is different from that in the crystalline phase. As an example, B diffusion in *a*-Si is mediated by defects in the

amorphous phase and has a complex B concentration dependence [195,196]. In *c*-Si, B diffusion is based on interactions with Si interstitials, but the diffusivity is much less than that in *a*-Si at the same temperature [197]. Hence, it is important to limit the time spent in the amorphous phase during SPE in such a situation. The interstitial-based mechanism also dominates the diffusion of P. In *c*-Ge, B diffusion is also mediated by Ge interstitials, but given the highly mobile nature of the vacancy in Ge, B is stubbornly immobile unless a source of interstitials is present, such as during irradiation [198]. In Ge, P, As, and Sb, diffusion is dominated by a vacancy-mediated process with only a negligible contribution of self-interstitials. Interestingly, a source of interstitials can act to suppress diffusion of such impurities.

7.6.2 Nondoping Impurities

Hydrogen in Si has received much attention for its widespread use in the fabrication of devices—from the passivation of defects to the formation of nanocavities in the ion-cut process. In the high-concentration regime, H plays a central role in the electronic and structural properties of amorphous Si and Ge [199]. The study of H diffusion in these materials has yielded important information about H-defect interactions and the nature of the *c*-*a* interface.

Hydrogen diffusion can be quite complex and is known to have a concentration dependence when present in concentrations greater than 2×10^{19} H/cm³ [200]. At higher concentrations, various microstructures can be formed during thermal processing, when H forms H₂ molecules and coalesces into nanobubbles [201]. The instability of H limits the thermal budget in high H concentration materials when H loss needs to be avoided. In the lower concentration regime, H diffusion has been characterized with an activation energy of 2.7 eV [200]. Interestingly, this is similar to the activation energy of SPE, suggesting that the two processes may have a similar rate-limiting mechanism. The diffusion of B and dangling bonds are also described by similar activation energies [195].

During SPE, H can infiltrate into the amorphous layer and segregate on the amorphous side of the *c*-*a* interface. This behavior is characteristic of impurities, rare earths, and many metals for which the segregation coefficient $k_{seg} \ll 1$. This is in contrast to many dopants in which $k_{seg} \approx 1$ and little segregation is observed. The segregated profile depends both on the velocity of the *c*-*a* interface and the diffusivity in the amorphous phase.

H infiltration can be enhanced by the presence of dopants in the amorphous phase because the diffusion coefficient is enhanced [202–204]. The mechanism appears to arise from a Fermi level effect. A trap limited diffusion model has been developed to describe the in-diffusion of H into surface amorphous Si layers during SPE and its segregation at the *c*-*a* interface. [205]

The infiltration of H has also been shown to be the cause of the so-called “asymmetric effect” in As-enhanced SPE, in which the As-enhanced SPE rate profile does not coincide with the As concentration profile [206]. At depths on either side of an implanted As

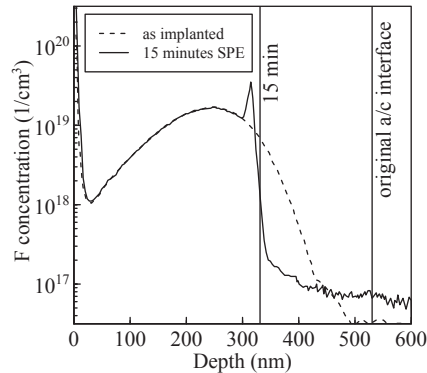


FIGURE 7.27 Secondary ion mass spectrometry profiles of fluorine (F) after implantation and after a 15-min anneal at 580 °C. The vertical lines indicate the crystalline–amorphous (*c–a*) interface positions. Data from Ref. [208].

profile with equivalent concentrations, the SPE rate is lower for the near-surface side of the profile [5]. These trends cannot be explained solely by the passivation of SPE defects at the *c–a* interface—that is, the effect is not additive [207]. There also appears to be some interaction with the As itself, either chemically or through the Fermi level, that also tends to affect the expected As-enhanced SPE rate.

A number of other nondoping impurities have also been used to control the diffusion of implanted dopants. It has been shown that transient enhanced diffusion can be reduced by inhibiting the release of interstitials from EOR defects. Both C and fluorine (F) can be used for this purpose because they act as traps for self-interstitials. F can be introduced via implantation of BF_2 molecules or implanted separately. Both C and F retard the SPE rate. As can be seen in Figure 7.27, the segregation of F at the *c–a* interface is quite significant [208–214]. The subsequent reduction in its total concentration reduces its trapping ability.

7.6.3 Metals

When present in the amorphous layer, metals such as iron, platinum, Au, and erbium enhance the SPE rate. This allows the anneal temperature to be lowered dramatically. Simultaneously, there can be significant segregation at the advancing *c–a* interface and redistribution of the metal. Nickel (Ni) in *a*-Si in particular displays an interesting concentration dependence. Below concentrations of 5×10^{18} Ni/cm³, Ni is incorporated into the *c*-Si substrate. In this case, no SPE rate enhancement is observed. Above this threshold, concentration segregation occurs, with the SPE rate increasing by up to 300 times [215,216]. During this process, nickel silicide (NiSi_2) precipitates in the *a*-Si at temperatures as low as 325–400 °C [217]. SPE is mediated by the precipitates and is thought to be induced by the free electrons of the metal, with the covalent Si bonds at the growing interface [218]. The formation of NiSi_2 via SPE requires much lower temperatures needed for the formation in *c*-Si [219]. Hence, this is an attractive pathway for

the realization of low-resistivity contacts and interconnects. Other compounds may also have other useful properties, such as the room-temperature ferromagnetism displayed by Mn_5Ge_3 germanides films on Ge (111) [220–222].

Other metals such as silver and Au do not react with the semiconductor to form compound phases such as silicides or germanides, but may lower the temperature required to initiate crystallization dramatically. In these cases, a eutectic is usually involved [223–225]. The process is also known as *metal-induced crystallization*. Crystallization events occur when atoms in the amorphous phase dissolve in the metal. After the atoms exceed some concentration, they precipitate onto the crystalline template. The metal is then pushed ahead of the advancing interface. Layer inversion or exchange can also take place during which an amorphous layer is deposited onto a metal layer, which is in turn deposited on a crystalline template (a process known as *aluminum-induced layer exchange*, because Al is most compatible with low-temperature processes) [226]. The substrate does not necessarily have to be *c*-Si. A broad range of other substrates have been considered including glass, ceramics, or polymer substrates.

7.7 SPE in Other Semiconductors

Si and Ge are model systems in which to study SPE and have great technological importance. However, SPE is used for the growth of a diverse range of unique systems. SPE in these systems can be complex and involve a number of other competing processes.

SPE in SiGe alloys is often concerned with strain effects and was the topic of many of the SiGe studies reviewed in [6]. Strain-free $\text{Si}_x\text{Ge}_{1-x}$ alloys were investigated by Kringhøj and Elliman with Ge contents ranging from 11 to 53 at.% [227]. Surprisingly, for the alloys between 11 at.% and 31 at.%, they found that the activation energy was greater than the value they measured for pure Si. This is in contrast to the expectation that the activation energy would decrease monotonically from a value of 2.70 eV for Si to 2.15 eV for Ge. This behavior was later confirmed by Haynes et al. [228]. A number of models have been proposed to understand these observations. By considering the presence of microscopic strain arising from changes in bond length, the activation energy trend could be reproduced with one scaling parameter [229]. Haynes et al. [228] proposed a model where the rate at which an atom will become part of the crystalline phase depends on its four nearest neighbors. This mechanism is consistent with the accepted model of defect formation and propagation along the *c*-*a* interface to assist bond rearrangements, provided that the SPE rate is determined by the propagation of these defects rather than their nucleation.

More exotic and complex crystalline materials also involve SPE in their formation. For example, amorphous LnCuOCh films can be deposited onto a (001)-oriented magnesium oxide substrate consisting of a 5-nm sacrificial Cu layer [230]. On annealing at 1000 °C, the Cu layer initiates epitaxial regrowth, and single-crystal LnCuOCh films are obtained [231]. The material is a transparent, wide-band gap semiconductor with promising

optical properties. The mechanism may be similar to that for Al-induced SPE mentioned earlier, and it is particularly suited to the epitaxial growth of complex oxides with a layered structure for which techniques such as conventional vapor-phase epitaxy are challenging. $\text{InGaO}_3(\text{ZnO})_m$ superlattices were the first of these types of materials to be grown [231].

7.8 Summary

In this chapter, we reviewed the crystallization behavior via SPE with a focus on Si and Ge materials. Both of these materials are of great technological importance and also serve as model systems in which to study SPE. The process can be described by a single activation energy of 2.7 eV and 2.15 eV, respectively, over the full range of temperatures that have been studied. For Si, this is up to its melting point. The single activation energy makes it attractive to consider that a single atomic mechanism may underlie this process over the full temperature range. Although this has never been determined explicitly, great insight has been gained through both experimental and theoretical efforts and models with great predictive power, taking into account orientation, doping and strain effects have been produced. Detailed observations of SPE substrate orientation, pressure, and impurity concentration dependencies are consistent with the following picture: A bond-breaking event occurs at $\langle 110 \rangle$ ledges on the $\{111\}$ c - a interfacial plane, which aids in the reconfiguration of atomic bonding during SPE regrowth, and the bond-breaking event is mediated by a structural defect, most likely the dangling bond.

Despite these observations, a definitive atomistic process has not been identified, and atomistic simulations have added complementary insight into the SPE process and have cast doubt on the existence of a single, simple rate-limiting step in the SPE process. Such simulations have shown that varied and complex atomic trajectories can be energetically favorable. The possible origin of a range of various SPE-related phenomena have also been identified, such as pressure and substrate orientation dependence. With continued advances in computational power and methods, it is expected that additional work in this area will yield further insight into the SPE process, with atomic-level information enabling better device design to be achieved.

Despite the lack of consensus on the exact nature of the atomic rearrangements that are the limiting step in the SPE process, the phenomenological model that has been developed through many years of studying the SPE process includes effects of substrate orientation, strain, and impurity concentration, and can be implemented in device fabrication codes. The model is also sensitive to subtle effects such as dopant-induced strain and dopant clustering. Such a kinetic model can be used for a broad range of experimental conditions. Currently, the formation of SPE-induced defects is not included in the model. Such defects play a role of increasing importance in both understanding the SPE phenomenon and optimizing the formation of future semiconductor devices. These defects arise at the original c - a interface depth, when two interfaces meet or when the impurity concentration exceeds some critical limit. They

also act as recombination centers and, more important, actively exchange interstitial defects with their immediate environment, giving rise, for example, to transient enhanced diffusion.

The inclusion of SPE as part of the standard process flow in the semiconductor industry signifies that our understanding of SPE kinetics will continue to be refined in a broader experimental framework and may also provide insight into other fundamental processes such as impurity diffusion and high-pressure phase transformations.

Acknowledgments

We acknowledge Greg Olson and John Roth for their seminal experimental work on SPE. We also thank Matthias Posselt, Benoit Sklenard, and Amelia C. Y. Liu, for stimulating discussions concerning the work presented in this chapter.

References

- [1] Leiberich A, Maher DM, Knoell RV, Brown WL. *Nucl Instrum Methods Phys Res Sect B* 1987;19/20:457.
- [2] Claverie A, Koffel S, Cherkashin N, Benassayag G, Scheiblin P. *Thin Solid Films* 2010;518:2307.
- [3] Csepregi L, Mayer JW, Sigmon TW. *Phys Lett* 1975;A54:157.
- [4] Mayer JW, Eriksson L, Picraux ST, Davies JA. *Can J Phys* 1968;46:663.
- [5] Olson GL, Roth JA. *Mat Sci Rep* 1988;3:1.
- [6] Olson G, Roth J. In: Hurlle D, editor. *Handbook of crystal growth*, vol. 3. Elsevier Science B.V; 1994. pp. 255–312. Chap. 7.
- [7] *International technology roadmap for semiconductors (itrs)*. San Jose: Semiconductor Industry Association; 2007.
- [8] Poate JM, Williams JS. *Ion implantation and beam processing*. Sydney: Academic Press; 1984.
- [9] Ziegler JF. *Ion implantation: science and technology*. Orlando: Academic Press; 1984.
- [10] Biersack JP, Haggmark LG. *Nucl Instrum Methods* 1980;174:257.
- [11] Posselt M. *Radiat Eff Defects Solids* 1994;87.
- [12] Holland OW, Appleton BR, Narayan J. *J Appl Phys* 1983;54:2295.
- [13] Stritzker B, Elliman RG, Zou J. *Nucl Instrum Methods Phys Res Sect B* 2001;193:175–7.
- [14] Romano L, Impellizzeri G, Tomasello MV, Giannazzo F, Spinella C, Grimaldi MG. *J Appl Phys* 2010;107:084314.
- [15] Kaiser R, Koffel S, Pichler P, Bauer A, Amon B, Claverie A, et al. *Thin Solid Films* 2010;518:2323.
- [16] Romano L, Impellizzeri G, Grimaldi M. *Mater Sci Semicond Process* 2012;15:703.
- [17] Bruno E, Scapellato GG, Bisognin G, Carria E, Romano L, Carnera A, et al. *J Appl Phys* 2010;108:124902.
- [18] Janssens T, Huyghebaert C, Vanhaeren D, Winderickx G, Satta A, Meuris M, et al. *J Vac Sci Technol B* 2006;24:510.
- [19] Lieten RR, Degroote S, Leys M, Posthuma NE, Borghs G. *Appl Phys Lett* 2009;94:112113.
- [20] Hung LS, Lau SS, von Allmen M, Mayer JW, Ullrich BM, Baker JE, et al. *Appl Phys Lett* 1980;37:909.
- [21] Morarka S, Rudawski NG, Law ME, Jones KS, Elliman RG. *J Appl Phys* 2009;105:053701.

- [22] Morarka S, Rudawski NG, Law ME, Jones KS, Elliman RG. *J Vac Sci Technol B* 2010;28:C1F1.
- [23] Darby BL, Yates BR, Ashish Kumara RGE, Kontosb Alex, Jones KS. *ECS Trans* 2013;50:753.
- [24] Ishiwarra H, Yamamoto H, Furukawa S, Tamura M, Tokuyama T. *Appl Phys Lett* 1983;43:1028.
- [25] Jellison Jr GE, Modine FA. *Appl Phys Lett* 1982;41:180.
- [26] Jellison Jr GE, Modine FA. *J Appl Phys* 1994;76:3758.
- [27] McCallum JC. *Appl Phys Lett* 1996;69:925.
- [28] Elliman RG, Wong WC. *Appl Phys Lett* 1996;69:2677.
- [29] Barvosa-Carter W, Aziz MJ, Phan A-V, Kaplan T, Gray LJ. *J Appl Phys* 2004;96:5462.
- [30] Feldman LC, Mayer JW, Picraux ST. *Materials analysis by ion channeling: submicron crystallography*. New York: Academic Press; 1982.
- [31] Chu WK, Mayer JW, Nicolet MA. *Backscattering spectrometry*. Orlando: Academic Press; 1978.
- [32] Bird JR, Williams JS. *Ion beams for materials analysis*. Australia: Academic Press; 1989.
- [33] Pelaz L, Marques LA, Barbolla J. *J Appl Phys* 2004;96:5947.
- [34] Laaziri K, Kycia S, Roorda S, Chicoine M, Robertson JL, Wang J, et al. *Phys Rev B* 1999;60:13520.
- [35] Etherington G, Wright A, Wenzel J, Dore J, Clarke J, Sinclair R. *J Non Cryst Solids* 1982;48:265.
- [36] Howie A. *Phil Mag* 2010;90:14.
- [37] Treacy MMJ, Gibson JM, Fan L, Patterson DJ, McNulty I. *Rep Prog Phys* 2005;68:2899.
- [38] Polk DE, Boudreaux DS. *Phys Rev Lett* 1973;31:92.
- [39] Car R, Parrinello M. *Phys Rev Lett* 1988;60:204.
- [40] Wooten F, Winer K, Weaire D. *Phys Rev Lett* 1985;54:1392.
- [41] Zachariasen W. *J Am Chem Soc* 1932;54:3841.
- [42] Lebedev AA. *Abr Staatl Opt Inst Leningrad* 1921;2.
- [43] Sadoc JF, Mosseri R. *Phil Mag* 1982;45:467.
- [44] Grigorovici R. *Electronic and structural properties of amorphous semiconductors*. London: Academic Press; 1973. Chap. The structure of amorphous semiconductors, pp. 192–241.
- [45] Treacy M, Gibson J, Keblinski P. *J Non Cryst Solids* 1998;231:99.
- [46] Voyles PM, Gerbi JE, Treacy MMJ, Gibson JM, Abelson JR. *Phys Rev Lett* 2001;86:5514.
- [47] Treacy MMJ, Borisenko KB. *Science* 2012;335:950.
- [48] Gibson JM, Treacy MMJ, Sun T, Zaluzec NJ. *Phys Rev Lett* 2010;105:125504.
- [49] Roorda S, Sinke WC, Poate JM, Jacobson DC, Dierker S, Dennis BS, et al. *Phys Rev B* 1991;44:3702.
- [50] Roorda S, Poate JM, Jacobson DC, Eaglesham DJ, Dennis BS, Dierker S. *Solid State Commun* 1990; 75:197.
- [51] Roorda S, Sinke WC, Scholte PMLO, van Loenen E. *Phys Rev Lett* 1989;62:1880.
- [52] Lu GQ, Nygren E, Aziz MJ. *J Appl Phys* 1991;70:5323.
- [53] Roorda S, Lavigreur Y. *Phil Mag* 2010;90:3787.
- [54] Acco S, Williams DL, Stold PA, Saris FW, van den Boogaard MJ, Sinke WC, et al. *Phys Rev B* 1996;53:4415.
- [55] Custer JS, Thompson MO, Jacobson DC, Poate JM, Roorda S, Sinke WC, et al. *App Phys Lett* 1994; 64:437.
- [56] Williamson DL, Roorda S, Chicoine M, Tabti R, Stolk PA, Acco S, et al. *App Phys Lett* 1995;67:226.
- [57] Biswas R, Kwon I, Bouchard AM, Soukoulis CM, Grest GS. *Phys Rev B* 1989;39:5101.

- [58] Spaepen F. *Acta Metall* 1978;26:1167.
- [59] Spaepen F, Turnbull D. *Laser and electron beam processing of semiconductor structure*. New York: Adcademic; 1981. p. 15.
- [60] Spaepen F. *Amorphous materials: modeling of structure and properties*. New York: TMS-AIME; 1983. p. 265.
- [61] Bernstein N, Aziz MJ, Kaxiras E. *Phys Rev B* 1998;58:4579.
- [62] da Silva CRS, Fazzio A. *Phys Rev B* 2001;64:075301.
- [63] Tu Y, Tersoff J, Grinstein G, Vanderbilt D. *Phys Rev Lett* 1998;81:4899.
- [64] Krzeminski C, Lampin E. *Eur Phys J B* 2011;290:283.
- [65] Spaepen F, Turnbull D. *Laser-solid interactions and laser processing*. In: *American Institute of physics conference proceedings*, New York: American Institute of physics; 1979. pp. 73–83.
- [66] Zellama K, Germain P, Squelard S, Bourgoin JC, Thomas PA. *J Appl Phys* 1979;50:6995.
- [67] Aziz MJ, Sabin P, Lu G. *Phys Rev B* 1991;44:9812.
- [68] Vineyard GH. *J Phys Chem Solids* 1957;3:121.
- [69] Aziz MJ. *Mat Res Soc Symp Proc* 1994;318:449.
- [70] Roth JA, Olson GL, Jacobson DC, Poate JM. *Appl Phys Lett* 1990;57:1340.
- [71] Johnson BC, Gortmaker P, McCallum JC. *Phys Rev B* 2008;77:214109.
- [72] Csepregi L, Kennedy EF, Mayer JW, Sigmon TW. *J Appl Phys* 1978;49:3906.
- [73] Williams J. *Nucl Instrum Methods* 1983;219(Part 1):209–10.
- [74] Darby BL, Yates BR, Martin-Bragado I, Gomez-Selles JL, Elliman RG, Jones KS. *J Appl Phys* 2013; 113:033505.
- [75] Custer JS, Battaglia A, Saggio M, Priolo F. *Phys Rev Lett* 1992;69:780.
- [76] Spaepen F, Turnbull D. *Laser annealing of semiconductors*. New York: Academic Press; 1982. Chap. Crystallization processes, pp. 15–42.
- [77] Custer JS. *Crucial issues in semiconductor materials and processing technologies*. Dordrecht: Kluwer Academic Publishes; 1992. pp. 477–482.
- [78] Rehtin MD, Pronko PP, Foti G, Csepregi L, Kennedy EF, Mayer JW. *Philos Mag A* 1978;37:605.
- [79] Lau SS, Vac J. *Sci Technol* 1978;15:1656.
- [80] Ho KT, Suni I, Nicolet M-A. *J Appl Phys* 1984;56:1207.
- [81] Csepregi L, Mayer JW, Sigmon TW. *Appl Phys Lett* 1976;29:92.
- [82] Chidambaram P, Bowen C, Chakravarthi S, Machala C, Wise R. *IEEE Trans Electron Devices* 2006; 53:944.
- [83] Saenger KL, Fogel KE, Ott JA, de Souza JP, Murray CE. *Appl Phys Lett* 2008;92:124103.
- [84] Rudawski NG, Jones KS, Gwilliam R. *Mater Sci Eng* 2008;R 61:40.
- [85] Lu GQ, Nygren E, Aziz MJ, Turnbull D. *Appl Phys Lett* 1990;56:137.
- [86] Chaki TK. *Phys Status Solidi A* 1994;142:153.
- [87] Fratello VJ, Hays JF, Spaepen F, Turnbull D. *J Appl Phys* 1980;51:6160.
- [88] Carter WB, Aziz MJ. *Mater Res Soc Symp Proc* 1995;356:87.
- [89] Rudawski NG, Jones KS, Gwilliam R. *Appl Phys Lett* 2007;91:172103.
- [90] Peteves SD, Abbaschian R. *Metall Trans A* 1991;22A:1271.
- [91] Rudawski NG, Jones KS. *Scr Mater* 2009;61:327.

- [92] Lai H, Cea SM, Kennel H, Dunham ST. *J Appl Phys* 2012;111:114504.
- [93] Lampin E, Krzeminski C. *J Appl Phys* 2009;106:063519.
- [94] Bernstein N, Aziz MJ, Kaxiras E. *Phys Rev B* 2000;61:6696.
- [95] Daw MS, Windl W, Carlson NN, Laudon M, Masquelier MP. *Phys Rev B* 2001;64:045205.
- [96] Aziz MJ. *Mater Sci Semicond Process* 2001;4:397.
- [97] Rudawski NG, Jones KS, Morarka S, Law ME, Elliman RG. *J Appl Phys* 2009;105:081101.
- [98] Barvosa-Carter W, Aziz MJ, Gray LJ, Kaplan T. *Phys Rev Lett* 1998;81:1445.
- [99] Sage JF, Barvosa-Carter W, Aziz MJ. *Appl Phys Lett* 2000;77:516.
- [100] Sage JF, Barvosa-Carter W, Aziz MJ. *J Appl Phys* 2006;99:113529.
- [101] Morarka S, Jin S, Rudawski NG, Jones KS, Law ME, Elliman RG. *J Vac Sci Technol B* 2011;29:041210.
- [102] Priolo F, Spinella C, Rimini E. *Phys Rev B* 1990;41:5235.
- [103] Kinomura A, Williams JS, Fujii K. *Phys Rev B* 1999;59:15214.
- [104] Ferlai AL, Cannavò S, Ferlai G, Campisano S, Rimini E, Servidori M. Proceedings of the fifth international conference on ion beam modification of materials. *Nucl Instrum Methods Phys Res Sect B* 1987;(Part 2):19–20. 470.
- [105] Williams JS, Elliman RG, Brown WL, Seidel TE. *Phys Rev Lett* 1985;55:1482.
- [106] Elliman R, Williams J, Brown W, Leiberich A, Maher D, Knoell R. Proceedings of the fifth international conference on ion beam modification of materials. *Nucl Instrum Methods Phys Res Sect B* 1987;(Part 2):19–20. 435.
- [107] Nakata J, Takahashi M, Kajiyama K. *Jpn J Appl Phys* 1981;20:2211.
- [108] Jackson KA. *J Mater Res* 1988;3:1218.
- [109] Fortuna F, Nédellec P, Ruault M, Bernas H, Lin X, Boucaud P. *Nucl Instrum Methods Phys Res Sect B* 1995;106:206.
- [110] Williams J, Azevedo GM, Bernas H, Fortuna F. In: Bernas H, editor. *Materials science with ion beams, topics in applied physics*, vol. 116. Berlin Heidelberg: Springer; 2010. pp. 73–111.
- [111] Gortmaker P. [Ph.D. thesis]. Australian National University; 1994.
- [112] Csepregi L, Kennedy EF, Gallagher TJ, Mayer JW, Sigmon TW. *J Appl Phys* 1977;48:4234.
- [113] Johnson BC, McCallum JC. *Phys Rev B* 2007;76:045216.
- [114] Suni I, Goltz G, Grimaldi MG, Nicolet M-A. *Appl Phys Lett* 1982;40:269.
- [115] Suni I, Goltz G, Nicolet M-A. *Thin Solid Films* 1982;93:171.
- [116] Williams JS, Elliman RG. *Phys Rev Lett* 1983;51:1069.
- [117] Lietoila A, Wakita A, Sigmon TW, Gibbons JF. *J Appl Phys* 1982;53:4399.
- [118] Mosley LE, Paesler MA. *J Appl Phys* 1985;57:2328.
- [119] Walser RM, Jeon Y-J. *Mater Res Soc Symp Proc* 1992;205:27.
- [120] Park WW, Becker MF, Walser RM. *Appl Phys Lett* 1988;52:1517.
- [121] Williams JS, Elliman RG. *Appl Phys Lett* 1980;37:829.
- [122] Bourgoin J, Lannoo M. *Point defects in semiconductors II*. Berlin: Springer; 1983.
- [123] McCallum JC. *Mater Res Soc Symp Proc* 1997;438:119.
- [124] McCallum JC. *Nucl Instrum Methods Phys Res Sect B* 1999;148:350.
- [125] Jeon Y-J, Becker MF, Walser RM. *Mater Res Soc Symp Proc* 1990;205:63.

- [126] D'Angelo D, Romano L, Crupi I, Carria E, Privitera V, Grimaldi MG. *Appl Phys Lett* 2008;93:231901.
- [127] Rudawski NG, Jones KS, Gwilliam R. *Appl Phys Lett* 2008;92:232110.
- [128] Johnson BC, Ohshima T, McCallum JC. *J Appl Phys* 2012;111:034906.
- [129] Pyykkö P, Atsumi M. *Chem Eur J* 2009;15:186.
- [130] Wortman JJ, Evans RA. *J Appl Phys* 1965;36:153.
- [131] Rudawski NG, Jones KS, Gwilliam R. *Phys Rev Lett* 2008;100:165501.
- [132] Barvosa-Carter W, Aziz MJ. *Appl Phys Lett* 2001;79:356.
- [133] Park W, Becker M, Walser RM. *Appl Phys Lett* 1988;52:1517.
- [134] Williams JS. *Nucl Instrum Methods Phys Res Sect B* 1983;209-210:219.
- [135] Trumbore FA. *Bell Syst Tech J* 1960;39:205.
- [136] Duffy R, Dao T, Tamminga Y, van der Tak K, Roozeboom F, Augendre E. *Appl Phys Lett* 2006;89:071915.
- [137] Jain SH, Griffin PB, Plummer JD, Mccoy S, Gelpey J, Selinger T, et al. *J Appl Phys* 2004;96:7357.
- [138] Chao Y-L, Prussin S, Woo JCS, Scholz R. *Appl Phys Lett* 2005;87:142102.
- [139] Posselt M, Schmidt B, Anwand W, Grotzschel R, Heera V, Mucklich A, et al. *J Vac Sci Technol B* 2008;26:430.
- [140] Duffy R, Venezia VC, van der Tak K, Hopstaken MJP, Maas GCJ, Roozeboom F, et al. *J Vac Sci Technol B* 2005;23:2021.
- [141] Juang MH, Cheng HC. *J Appl Phys* 1992;72:5190.
- [142] Pawlak BJ, Surdeanu R, Colombeau B, Smith AJ, Cowern NEB, Lindsay R, et al. *Appl Phys Lett* 2004;84:2055.
- [143] Pawlak BJ, Duffy R, Janssens T, Vandervorst W, Maex K, Smith AJ, et al. *Appl Phys Lett* 2005;87:031915.
- [144] Satta A, Simoen E, Clarysse T, Janssens T, Benedetti A, Jaeger BD, et al. *Appl Phys Lett* 2005;87:172109.
- [145] Hamilton J, Collart E, Colombeau B, Jeynes C, Bersani M, Giubertoni D, et al. *Nucl Instrum Methods Phys Res Sect B* 2005;237:107.
- [146] Pawlak BJ, Vandervorst W, Smith AJ, Cowern NEB, Colombeau B, Pages X. *Appl Phys Lett* 2005;86:101913.
- [147] Saito T, Ohdomari I. *Philos Mag B* 1984;49:471.
- [148] Polk DE, Non-Cryst J. *Solids* 1971;5:365.
- [149] Kugler S, Pusztai L, Rosta L, Chieux P, Bellissent R. *Phys Rev B* 1993;48:7685.
- [150] Biswas P, Atta-Fynn R, Drabold DA. *Phys Rev B* 2004;69:195207.
- [151] Marqués LA, Pelaz L, Aboy M, Enríquez L, Barbolla J. *Phys Rev Lett* 2003;91:135504.
- [152] Cook SJ, Clancy P. *Phys Rev B* 1993;47:7686.
- [153] Luedtke WD, Landman U. *Phys Rev B* 1989;40:1164.
- [154] Kluge MD, Ray JR, Rahman A. *Phys Rev B* 1987;36:4234.
- [155] Hugouvieux V, Farhi E, Johnson MR, Juranyi F, Bourges P, Kob W. *Phys Rev B* 2007;75:104208.
- [156] Lopez P, Pelaz L, Marques LA, Santos I. *J Appl Phys* 2007;101:093518.
- [157] Martin-Bragado I. Proceedings of the 11th computer simulation of radiation effects in solids (COSIRES) conference Santa Fe, New Mexico, USA, July 24–29, 2012. *Nucl Instrum Methods Phys Res Sect B* 2013;303:184.

- [158] Martin-Bragado I, Sklenard B. *J Appl Phys* 2012;112:024327.
- [159] Martin-Bragado I, Moroz V. *Appl Phys Lett* 2009;95:123123.
- [160] Motooka T, Nishihira K, Munetoh S, Moriguchi K, Shintani A. *Phys Rev B* 2000;61:8537.
- [161] Stillinger FH, Weber TA. *Phys Rev B* 1985;31:5262.
- [162] Gärtner K, Weber B. *Nucl Instrum Methods Phys Res Sect B* 2003;202:255.
- [163] Krzeminski C, Brulin Q, Cuny V, Lecat E, Lampin E, Cleri F. *J Appl Phys* 2007;101:123506.
- [164] Marques LA, Caturla M-J, de la Rubia TD, Gilmer GH. *J Appl Phys* 1996;80:6160.
- [165] Weber B, Stock D, Gärtner K. *Nucl Instrum Methods Phys Res Sect B* 1999;148:375.
- [166] Posselt M, Gabriel A. *Phys Rev B* 2009;80:045202.
- [167] Munetoh S, Moriguchi K, Shintani A, Nishihira K, Motooka T. *Phys Rev B* 2001;64:193314.
- [168] Motooka T. *Mater Sci Eng A* 1998;253:42.
- [169] Albenze EJ, Clancy P. *Mol Simul* 2005;31:11.
- [170] Lenosky TJ, Sadigh B, Alonso E, Bulatov VV, de la Rubia TD, Kim J, et al. *Modell Simul Mater Sci Eng* 2000;8:825.
- [171] Shanavas KV, Pandey KK, Garg N, Sharma SM. *J Appl Phys* 2012;111:063509.
- [172] Kerrache A, Mousseau N, Lewis LJ. *Phys Rev B* 2011;84:014110.
- [173] Marques LA, Pelaz L, Santos I, Lopez P, Duffy R. *J Appl Phys* 2012;111:034302.
- [174] Lampin E, Krzeminski C. *J Appl Phys* 2011;109:123509.
- [175] Mattoni A, Colombo L. *Phys Rev B* 2004;69:045204.
- [176] Narayan J, White CW, Holland OW, Aziz MJ. *J Appl Phys* 1984;56:1821.
- [177] Thompson MO, Galvin GJ, Mayer JW, Peercy PS, Poate JM, Jacobson DC, et al. *Phys Rev Lett* 1984; 52:2360.
- [178] Tersoff J. *Phys Rev B* 1988;37:6991.
- [179] What Lampin and coworkers call interface “diffuseness,” most authors call “roughness.” In a diffuse interface, there are many layers of atoms with properties (e.g., coordination, enthalpy) intermediate between those of the atoms in the two bulk phases. In a rough but sharp interface, there are very few such atoms; but, if the “height” coordinate is normal to the plane of the average interface, the height at the transition in properties varies significantly with lateral position.
- [180] Drosd R, Washburn J. *J Appl Phys* 1982;53:397.
- [181] Jones KS, Prussin S, Weber ER. *Appl Phys A* 1988;45:1.
- [182] Nishikawa S, Tanaka A, Yamaji T. *Appl Phys Lett* 1992;60:2270.
- [183] Liu ACY, McCallum JC. *Mater Sci Eng B* 2003;97:167.
- [184] Liu ACY, McCallum JC, Wong-Leung J. *J Mater Res* 2001;16:3229.
- [185] Liu ACY, McCallum JC, Wong-Leung J. *Nucl Instrum Methods Phys Res Sect B* 2001;175-177:164.
- [186] Duffy R, Dal MJHV, Pawlak BJ, Kaiser M, Weemaes RGR, Degroote B, et al. *Appl Phys Lett* 2007;90: 241912.
- [187] Duffy R, Shayesteh M, McCarthy B, Blake A, White M, Scully J, et al. *Appl Phys Lett* 2011;99:131910.
- [188] Saenger KL, de Souza JP, Fogel KE, Ott JA, Sung CY, Sadana DK, et al. *J Appl Phys* 2007;101:024908.
- [189] Saenger KL, Fogel KE, Ott JA, Sung CY, Sadana DK, Yin H. *J Appl Phys* 2007;101:084912.
- [190] Morarka S, Rudawski NG, Law ME. *J Vac Sci Technol B* 2008;26:357.
- [191] Narayan J. *J Appl Phys*. 1982;53:8607.

- [192] Zhu X. Nano/micro engineered and molecular systems. In: NEMS '06. 1st IEEE international conference on newspace, 470 (2006); 2006.
- [193] Zhu X, Williams JS, Llewellyn DJ, McCallum JC. *Appl Phys Lett* 1999a;74:2313.
- [194] Zhu X, Williams J, McCallum J. *Nucl Instrum Methods Phys Res Sect B* 1999;148:268.
- [195] Mirabella S, Salvador DD, Bruno E, Napolitani E, Pecora EF, Boninelli S, et al. *Phys Rev Lett* 2008; 100:155901.
- [196] Mirabella S, Salvador DD, Napolitani E, Bruno E, Priolo F. *J Appl Phys* 2013;113:031101.
- [197] Duffy R, Venezia VC, Heringa A, Pawlak BJ, Hopstaken MJP, Maas GCJ, et al. *Appl Phys Lett* 2004; 84:4283.
- [198] Bracht H, Schneider S, Klug JN, Liao CY, Hansen JL, Haller EE, et al. *Phys Rev Lett* 2009;103:255501.
- [199] Street RA. *Physica B* 1991;170:69.
- [200] Roth JA, Olson GL, Jacobson DC, Poate JM. *Mat Res Soc Symp Proc* 1993;297:291.
- [201] Acco S, Williamson DL, van Sark WGJHM, Sinke WC, van der Weg WF, Polman A, et al. *Phys Rev B* 1998;58:12853.
- [202] Johnson BC, Caradonna P, McCallum JC. *Mater Sci Eng B* 2009;157:6.
- [203] Johnson BC, Caradonna P, Pyke DJ, McCallum JC, Gortmaker P. *Thin Solid Films* 2010;518:2317.
- [204] Johnson BC, Atanacio AJ, Prince KE, McCallum JC. *Mat Res Soc Symp Proc* 2008;1070:4.
- [205] Johnson BC, Mastromatteo M, Salvador DD, Napolitani E, Carnera A, McCallum JC. *ECS Trans* 2010;33:157.
- [206] Johnson BC, McCallum JC. *J Appl Phys* 2004;95:4427.
- [207] Johnson BC, McCallum JC. *J Appl Phys* 2004;96:2381.
- [208] Mirabella S, Impellizzeri G, Bruno E, Romano L, Grimaldi MG, Priolo F, et al. *Appl Phys Lett* 2005; 86:121905.
- [209] Mastromatteo M, De Salvador D, Napolitani E, Panciera F, Bisognin G, Carnera A, et al. *Phys Rev B* 2010;82:155323.
- [210] Mokhberi A, Kasnavi R, Griffin PB, Plummer JD. *Appl Phys Lett* 2002;80:3530.
- [211] Downey DF, Chow JW, Ishida E, Jones KS. *Appl Phys Lett* 1998;73:1263.
- [212] Lopez GM, Fiorentini V, Impellizzeri G, Mirabella S, Napolitani E. *Phys Rev B* 2005;72:045219.
- [213] Panciera F, Hoummada K, Mastromatteo M, Salvador DD, Napolitani E, Boninelli S, et al. *Appl Phys Lett* 2012;101:103113.
- [214] Boninelli S, Impellizzeri G, Priolo F, Napolitani E, Spinella C. *Nucl Instrum Methods Phys Res Sect B* 2012;282:21.
- [215] Mohadjeri B, Linnros J, Svensson BG, Östling M. *Phys Rev Lett* 1992;68:1872.
- [216] Kuznetsov AY, Svensson BG, Nur O, Hultman L. *J Appl Phys* 1998;84:6644.
- [217] Hayzelden C, Batstone JL. *J Appl Phys* 1993;73:8279.
- [218] Spaepen F, Nygren E, Wagner AV. *Crucial issues in semi-conductor materials and processing technologies, NATO ASI series e: applied sciences*. Dordrecht: Kluwer Academic; 1992. p. 483.
- [219] Nicolet M-A, Lau SS. *VLSI electronics microstructure sciences*. New York: Academic; 1983. Chap. 6, p. 343.
- [220] Hirvonen Grytzeliuss J, Zhang HM, Johansson LSO. *Phys Rev B* 2012;86:125313.
- [221] Sangaletti L, Magnano E, Bondino F, Cepek C, Sepe A, Goldoni A. *Phys Rev B* 2007;75:153311.
- [222] Zeng C, Erwin SC, Feldman LC, Li AP, Jin R, Song Y, et al. *Appl Phys Lett* 2003;83:5002.

- [223] Konno TJ, Sinclair R. *Mater Sci Eng A* 1994;426(Part 1):179–80.
- [224] Konno TJ, Sinclair R. *Philos Mag B* 1992;66:749.
- [225] Gestel DV, Dogan P, Gordon I, Bender H, Lee K, Beaucarne G, et al. *Mater Sci Eng B* 2009;134:159–60.
- [226] Wang JY, Wang ZM, Mittemeijer EJ. *J Appl Phys* 2007;102:113523.
- [227] Kringhøj P, Elliman R. *Phys Rev Lett* 1994;73:858.
- [228] Haynes TE, Antonell MJ, Lee CA, Jones KS. *Phys Rev B* 1995;51:7762.
- [229] Kringhøj P, Elliman R, Fyhn M, Shiryaev S, Larsen AN. *Nucl Instrum Methods Phys Res Sect B* 1995;106:346.
- [230] Hiramatsu H, Ohta H, Suzuki T, Honjo C, Ikuhara Y, Ueda K, et al. *Cryst Growth Des* 2004;4:301.
- [231] Ohta H, Nomura K, Orita M, Hirano M, Ueda K, Suzuki T, et al. *Adv Funct Mater* 2003;13:139.